INTERNATIONAL TABLES FOR CRYSTALLOGRAPHY

ISSN 1574-8707
it.iucr.org

Volume I, X-ray Absorption Spectroscopy and Related Techniques
ISBN: 978-1-119-43394-1

Chapter 3.14

Keywords: sample absorption; sample thickness; accuracy.

Accurate data: mapping sample absorption and thickness effects

Stephen P. Best[a]* and Christopher T. Chantler[b]

[a]School of Chemistry, University of Melbourne, Parkville, Victoria 3010, Australia, and [b]School of Physics, University of Melbourne, Parkville, Victoria 3010, Australia. *Correspondence e-mail: spbest@unimelb.edu.au

The systematic and random errors associated with any measurement are dependent upon experimental design and directly, or indirectly, constitute a compromise between the physics of the measurement, the questions to be addressed and the beamtime available. The processing of experimental measurements to correct for instrumental and sample-dependent phenomena so as to obtain observations with a defined accuracy underpins any subsequent analysis and assessment of the reliability of the conclusions. Here, strategies for the correction and statistical analysis of experimental data are presented, yielding point-by-point estimates of the measured accuracy which can then be used to assess alternate models of the coordination geometry of the absorbing atom. A particular focus is placed on sample absorption and thickness effects. These methods are particularly valuable for the study of species at low concentration and sample forms lacking long-range order.

1. Introduction

Analytical methods describe protocols which, when implemented, yield results with a quantified accuracy and are valuable because they can be communicated and accepted by others inside and outside the field. During the development of experimental methods there is a period of instrumental, computational and sampling advances which significantly increase the quality–cost quotient. When the method is mature, the balance shifts from method development to applications, including a more advanced understanding of signal and information content. Methods such as IR, UV–Vis and NMR spectroscopy, gas chromatography, mass spectrometry and laboratory-based small-angle X-ray scattering (SAXS) and X-ray diffraction (XRD) may be argued to fall into this mature category. X-ray absorption spectrospcopy (XAS) does not yet fit into the mature category and is a field that is undergoing exciting dynamic development.

XAS experiments are highly demanding and the establishment of beamlines that allow the routine collection of spectra is a significant achievement that is too often taken for granted by the user community. In what we define as conventional operation, the beamline is optimized at different times during the user cycle, but uncertainty estimation and the measurement of diagnostics of systematic errors are not embedded into the measurement of individual spectra. Depending on the stability of the beamline and its associated electronics, such an approach can allow the efficient collection of spectra by a higher number of users on oversubscribed beamlines; however, such an approach does not allow the quantification of systematic errors. Measurements of this sort do not have a statistically defined uncertainty. High-accuracy measurements of XAS spectra may be categorized as those where individual observations within a spectrum are obtained with a measured

Related chapters

Volume I: 3.13, 3.38, 3.39, 3.42, 3.46, 3.47, 4.6, 4.7

precision and accuracy (Creagh & Hubbell, 1987, 1990; Chantler *et al.*, 1999). Conventional practices encompass a broad range of strategies which differ according to the purpose to which the measurements will be applied. This extends from pattern matching, 'fingerprinting' (see Fujikawa, 2024; Fornasini, 2024; Webb, 2024) and multi-component analysis (principal component analysis; Webb, 2024; Webb & Gaillard, 2015) to structural analysis in the region close to the absorbing atom (Liu & Frenkel, 2024). Physical limitations (solution phase, sample size, heterogeneity, active species concentration and radiation sensitivity) associated with the sample can restrict the approaches which may be applied to data collection and this can limit the statistical precision and the accuracy of the measurement (see Bunker, 2024*a*; Heald, 2024). Sample-based limitations are compounded by the serious time pressure associated with access to XAS beamlines at advanced synchrotrons. In response to this, it has been commented by numerous beamline scientists, for example at the Q2XAFS 2017 meeting (Diaz-Moreno & Strange, 2018) and the IUCr Congress 2017 (*Abstracts of the XXIV IUCr Congress*; https://journals.iucr.org/a/issues/2017/a2/00/), that it is important to establish accepted criteria for assessment of the quality of XAFS data sets.

High-accuracy measurements (for example the X-ray extended-range technique; XERT; Chantler, 2009; Tantau *et al.*, 2014) provide the high-quality data that are needed to test and develop theory and analytic techniques. The methods used in such studies necessarily have strict requirements in terms of defining both the signal and the contributions to the noise and from systematic errors. At each energy point of the spectrum, the beam (energy and harmonic content; Tran, Barnea *et al.*, 2003; Barnea *et al.*, 2011), detection system (background current), scattering and linearity of the absorption measurement (Chantler, 2001; Tran, de Jonge *et al.*, 2004) are assessed by measurements with sufficient repeats to allow statistical analysis, the determination of artefacts and systematics, the quantification of uncertainty and the propagation of uncertainties (Chantler, Tran, Paterson, Cookson *et al.*, 2000). When combined with detailed sample characterization, including inhomogeneity, sample mapping (de Jonge *et al.*, 2004*a*; Tran, Chantler *et al.*, 2004) and nano-roughness (Glover *et al.*, 2009), this technique provides a measurement of the absolute mass attenuation coefficient with high accuracy and precision. It also provides high-accuracy relative XAS spectra for the analysis of any component of the spectral parameters in the EXAFS, XANES or pre-edge analysis. Ideal samples are needed for high-accuracy measurements of the mass attenuation coefficient within and outside the XAFS and edge region; this is most conveniently obtainable for metal foils, crystals, uniform homogeneous solids and glasses measured in transmission mode.

In principle, measurements are possible with both transmission and fluorescence detection from pure, concentrated and dilute samples. In practice, the sample environment provides strict limits as to the measurement process and demands alternative approaches for optimum data quality in a defined time period.

Many groups have contributed to the drive for high accuracy from XAS measurements and to the consideration of sources of uncertainty and systematic errors. The broader XAS community, led by beamline scientists, has actively participated in the evolution of the technique over the last 30–40 years (Nordfors, 1960; Barnea & Mohyla, 1974; Lee *et al.*, 1981; Goulon *et al.*, 1982; Oyanagi, 1988; Zhang *et al.*, 1996; Creagh & Hubbell, 1987, 1990) and this has been supplemented by analysis packages including, for example, *GNXAS* (Westre *et al.*, 1995; Filipponi, Di Cicco *et al.*, 2024; Filipponi, Natoli *et al.*, 2024) and *Athena*/*Artemis*, which is enriched by the Ravel and Newville notes, blogs, GitHubs and *IFEFFIT* digests (Newville, 2001*a*,*b*; Ravel & Newville, 2005, 2024). Similarly, work on data-analysis development and technique has led to significant advances (Krappe & Rossner, 1999, 2000, 2002), which yet concluded that a 'severe drawback of any error analysis is the considerable uncertainty in associating an 'experimental' error with the input EXAFS function χ'.

Later work proposed how to define and implement a possible background subtraction in a method improved from a simple spline (Krappe & Rossner, 2004) and how to avoid Fourier filtering or the use of a Nyquist theorem (Rehr *et al.*, 2005). Other work developed the method of calibrated relative XAS measurements to probe small bond changes with, for example, temperature (Pettifer *et al.*, 2005; Abd el All *et al.*, 2013; Gianolio *et al.*, 2013). The calibration of energy, including at multiple points during a data collection, has been emphasized (Tran *et al.*, 2024), together with the measurement of dark current and dead-time correction (Diaz-Moreno, 2012). Recent work has emphasized the possibilities provided by monochromator Bragg glitches (three-beam diffraction) as an important diagnostic of energy calibration which can yield information on monochromator and sample orientation (Sutter *et al.*, 2016). Whereas monochromator glitches can seriously degrade fluorescence data collection, proper transmission measurement should cancel monochromator intensity excursions but remain susceptible to perfect crystal sample Bragg reflections (Tran, Chantler *et al.*, 2003). Other recent developments have presented some exciting opportunities in this space (Chantler, Islam *et al.*, 2012; Vaarkamp, 1998; Trevorah *et al.*, 2019). Useful summaries of some of these developments are given in Koningsberger & Prins (1988) and Bunker (2010).

A strong point has been made by Curis *et al.* (2005) arguing that data fitting and analysis is more sensitive and insightful if the point precision is used and included in the data-point uncertainty; that is, if some direct estimate of the statistical error is made and propagated in error analysis. In other words, high-accuracy techniques provide additional insight and more physical parametrization. Most least-squares, maximum-likelihood, Bayesian and Monte Carlo analysis techniques assume that the experimental data points are independent. This is not true for fitting in Fourier space or for any Fourier filtering, but it can be true in experimental (k) space (Vaarkamp, 1998). In a second paper, this group noted the importance of dealing with systematic effects, including harmonics, thickness effects and self-absorption (Curis *et al.*,

Table 1
Summary of the main characteristics of the approaches used to collect XAS spectra for structural analysis.

	High accuracy, *e.g.* XERT (Chantler, 2009; Tantau *et al.*, 2014)	Hybrid	Conventional
Energy-dependent values of the mass extinction coefficient	Each measurement has an independently determined accuracy and precision	Each measurement has an independently determined precision including measurements of systematic variation contributing to variance sampling	No formal estimate of precision or accuracy, but repeats of scans or multiple independent pixels or an estimate of precision based on noise across a local region of the overall spectrum
Samples	Ideal: solids, metals, crystals, concentrated solutions	Solids, concentrated solutions and dilute solutions	Solids, concentrated, dilute and ultradilute solutions
Measurement type	Transmission or fluorescence	Transmission or fluorescence	Transmission or fluorescence, rapid (continuous) scan
Diagnostics and systematic contributions, corrections, energy	Measured, multiple energies (10–20)	Measured, multiple energies (2–4)	One edge point from a reference metal foil
Harmonic	Measured	Measured	Not measured
Scattering	Measured	Measured	Not measured
Self-absorption	Measured, multiple sample attenuations	Measured, multiple sample attenuations	Single observation, empirical fit
Multiple element fluorescence	Each channel corrected for self-absorption. Calibration of fluorescence detector and pixels.	Each channel corrected for self-absorption. Calibration of fluorescence detector and pixels.	Weighted average sometimes based on edge step height
Error analysis	Both energy and mass absorption coefficient	Energy and mass absorption coefficient	
Relative time	5–8	3–6	1

2005), which is an important focus of this contribution (Section 4).

All of these developments are important, yet are often perceived as specialized techniques and applications by particular research groups on a particular beamline. As such, their value and significance needs to be more widely articulated and implemented by the worldwide community so that these advances can be implemented and available to all users. Beamline modes of operation which allow the collection of data with quantified accuracy should be a key design criterion for new beamlines.

The demands of high-accuracy measurements are not easily accommodated for most samples examined in a general beamline program, and lie outside the focus of the current chapter, which is the development of approaches which allow measurements with high relative accuracy from conventional samples; that is, the extraction of the relative mass extinction coefficient. Accurate measurements of this sort require the quantification of systematic errors with rigorous point-by-point error analysis embedded into the collection of spectra, and a hybrid of the methods used for the collection of conventional and high-accuracy spectra is required. Operationally, the distinction between conventional and high-accuracy measurements is subjective and the characteristics of these classes (in the minds of the authors) are summarized in Table 1. For convenience, the term hybrid techniques has been used to describe methods for the collection of XAS spectra which, while not satisfying all of the expectations and requirements for highest accuracy, provide a means of acquiring spectra with an estimate of the precision and relative accuracy of each data point (Chantler *et al.*, 2015). The most important differences between hybrid techniques compared with the more exacting XERT methodologies relate to the need to accommodate solutions or dilute samples at ambient temperature or in cryogenic sample environments (Chantler *et al.*, 2015; Islam *et al.*, 2016; Chantler, Barnea *et al.*, 2012). The determination of the relative and absolute XAS with high and defined accuracy and precision from dilute solutions and disordered solids in strongly attenuating matrices using hybrid techniques is designed to allow a more quantitative analysis of dilute samples where the composition is ill-defined or where fluorescence detection might be conventionally considered to be essential. Hybrid techniques give data with defined accuracy with fewer experimental demands than required for high-accuracy measurements. This can, for example, be important for low-temperature measurements in standard cryostats. Hybrid techniques also provide a conduit for the transfer of approaches developed in high-accuracy measurements to conventional techniques, although care should be taken in the use and calibration of any reference standards. The key changes in measurement technique relate to using a well defined reference standard separately from the samples, and redefining the interpretation of multiple sample measurements and mapping.

2. Measurement protocols

2.1. The sample and sampling protocols

An ideal starting point for any measurement is the presentation of a well defined, well characterized homogeneous sample of appropriate thickness, density, composition and concentration. Overviews of the requirements and strategies for sample preparation are available in monographs (Calvin, 2013), which are commonly supplemented by guidance from the different beamline teams. Clearly, samples which are inhomogeneous on the micrometre scale (roughness, wedges or curved surfaces) or discontinuous (pinholes or cracking) will give more challenging spectra subject to ill-defined distortions arising from time-dependent translation of the sampling volume during the collection of the spectrum.

Solution or frozen solution samples can give homogeneous samples, but photolysis/photoreduction of the solute and crystallization of solvent during the generation of frozen solutions are potential complications. In general, a flat metal foil or a well defined crystal is still inhomogeneous on the micrometre scale, so methodologies of XERT are required to characterize them and the ensuing systematics to yield high accuracy. This is no less the case for solution or frozen solution samples.

A critical requirement in hybrid techniques is assessment of the error of the individual points of the spectrum. In effect, this typically requires point-by-point measurement in which blank, background, scattering and multiple sample measurements are conducted at each energy step using samples with multiple concentrations or thicknesses. Further, measurements related to beam quality (scattering, harmonic component and energy) are needed to correct for key systematic errors. Repeated measurement of data points is a common requirement for all XERT and hybrid applications, with preferably towards ten repeat measurements of each sample, blank or reference. Published protocols for data collection and error propagation for transmission measurements are summarized in Section 3.

The measurement of dilute samples is a requirement that is common to the majority of XAS investigations extending over all discipline areas. In this context, 'dilute' is interpreted to span the range from 0.5 to 10 mM for first-row transition metals (*i.e.* ∼25–500 p.p.m.). In conventional wisdom, this corresponds to samples for which transmission measurements are either not practicable or give very poor spectra compared with those obtained using fluorescence detection. Notwithstanding this prejudice, transmission measurements can remain competitive at lower concentrations and, importantly, provide the experimental information needed for normalization of the fluorescence signal. Multi-element germanium detectors are most commonly employed at XAS beamlines, largely due to their sensitivity, energy discrimination and large solid area of detection. In conventional experiments, detectors of this sort are used to provide a single averaged output, although the processing of this output signal is not entirely straightforward. In hybrid experiments the individual detector pixel elements are independent observations which are used to extract both the signal and its associated uncertainty. As discussed in later sections, the energy-dependent normalization of individual detector elements complicates data processing but has the advantage of providing a statistical basis for assessing the uncertainty of the individual spectral data points.

The strategies outlined here apply to transmission and to fluorescence measurements, to high-accuracy (XERT) and to intermediate advances and developments (hybrid), and to second-generation (bending-magnet) beamlines and to advanced third-generation beamlines, for example wigglers and undulators. The implementation of the principles described herein are, of course, highly beamline-specific and need to be commensurate with the objectives of the application.

2.2. Cryogenic measurements

Photodamage, principally photoreduction, is an ever-present hazard in XAS measurements, especially for dilute, fragile or biological samples, and cryogenic methods are commonly used to mitigate these effects sufficient to allow the collection of spectra over a useful k-range. A critical requirement of hybrid measurements is the illumination of multiple sample positions at each energy point. This can generally be achieved by physical translation of the cryostat to allow the interrogation of sample positions within the clear aperture provided by the entrance and exit windows (typically ∼30 mm in diameter). The pressure differential implies that exterior cryostat windows are not flat, and cryostat designs often expect a curved profile for the radiation-shield windows. These effects lead to small differences in the background absorption which are dependent on the cryostat position. The differences are small and are typically 1–2% of the absorption due to the Kapton windows and the air path which, in turn, are small corrections to the absorption cross-section.

The physical restrictions on the area available for samples/references imposed by the cryostat geometry impact significantly on the experiment design. Individual samples will ideally have dimensions sufficient to allow the measurement of spectra from at least three non-overlapping regions, limiting the number of samples able to be studied in a single experiment. For solution samples, it is challenging to achieve a compact placement of solution wells, which is compounded when it might be necessary to choose solvents which prevent the use of self-adhesive Kapton windows. Strategies for dealing with this problem are available in the literature (Chantler *et al.*, 2015). Alternate approaches include the assembly of pre-frozen solution samples or the implementation of a strategy in which the sample is translated while the cryostat remains static.

Unlike conventional measurements, which involve sample movement at the completion of spectral acquisition, hybrid measurements are typically conducted in a single energy scan with translation of the cryostat typically to 4–8 different positions at each energy with repeats (three sample, three dilute sample, one background and one blank). While the travel for each movement is comparatively small, the reliability of the stepper motors driving the cryostat stage is an important and beamline-dependent consideration. Further, each measurement should consist of sufficient repeat observations, preferably ∼10, so as to allow statistical estimation of the measurement variance.

2.3. Data collection

An advantage of hybrid measurements is the potential to optimize the data-collection strategy according to the requirements of the experiment and as a function of k or E. At each energy point measurements of beam or sample diagnostics may be conducted, and this can be implemented at an energy spacing that matches the strengths or limitations of the beamline and the information content of the sample XAS spectrum being collected (*i.e.* the XAFS oscillations,

resolution, structure *etc.*). This approach can, for example, include measurement of multiple calibration foils (Chantler, Islam *et al.*, 2012), recognize measurements where high I_0 (for example monochromator glitches) or I_f (for example Bragg diffraction) intensity would otherwise lead to unusable data, and either apply correction protocols or alter the energy of the measurement (Tran, Chantler *et al.*, 2003; Sutter *et al.*, 2016) or simply provide reliable stop and restart protocols following beam loss (Chantler, Tran, Paterson, Barnea *et al.*, 2000).

2.4. Cost–benefit analysis

A beamline or facility manager may question the cost of building and designing an endstation to achieve accuracy or precision, pre-processing software and investing time in the pre-processing of data to automate the determination of precision and pointwise variance. The benefit is often well defined data quality and potentially accuracies some 10–100 times previous convention. This seems to be a simple argument and a valid priority. Once implemented, as a specialized experiment or as a routine facility option, operational considerations come into play. There is a real cost in experimental beamtime allocation and investigation for defining data quality using hybrid or high-accuracy techniques, for the proposer, for the expected time for a *de novo* experiment and for the increased time for a routine well set up beamline mode for XAFS; for example, in comparison to a standard beamtime XAFS, XANES or a pre-edge fingerprint comparison. In many cases a simple XANES fingerprinting is effective and valuable, although conclusions without EXAFS analysis are more liable to give incorrect answers. Hence, the quest for greater insight and greater validity of conclusions should lead us to new technology and implementation.

Theoretical errors can still often dominate in particular regions, especially at low k, which can be cited as a reason for not bothering to collect data of defined quality; yet many experiments seeking to develop our understanding of particular systems or to develop theory or find new physics need this information and insight. Equally, extracting the XAFS using E_0, splines and other techniques can introduce large and systematic errors in parameters, especially at low k. It remains very important to try to better define uncertainties or optimize data-collection techniques in order to define data quality more carefully. The discussions of this chapter do not address all possible systematics (if indeed they were known) so one could be concerned that for a particular application there may be a specific failure of current or developing methods. The solution to this meta-question is to fix known systematic issues and then to fix more. This is always a work in progress.

The cost–benefit analysis of the data-collection strategies hinge on the time side of the equation (Table 1). Whilst any such comparison is highly dependent on the sample, a reasonable estimate of the increase in time required for optimized hybrid measurements of XAS spectra relative to conventional methods is a factor of approximately 3 or 6, depending on whether the diluted form of the sample is counted separately. Approximately half of this difference is accounted for by the time required to collect beam and detector diagnostics and these carry the greatest time overhead in the first measured spectrum. With the improved beamline diagnostics provided by experiments of this type, it is possible to more efficiently utilize observations of these diagnostics between runs and lower the time penalty. The major gains in the accuracy and reliability of the data can be achieved without a significant increase in beam-on-sample time. Case studies which illustrate both the protocols for establishing the uncertainties of the individual data points and potential improvements in the quality and the reliability of the analysis are given in Section 6.

3. Constitutive equations and physics for transmission

Consider a typical application to a dilute frozen solution in a cryostat, with multiple (three) cells using XAFS in transmission, with 15 m*M* solute, 1.5 m*M* solute and pure solvent in the respective cells.

Experimentally, absorption is conventionally (formally) given by the Beer–Lambert equation,

$$I = I_0 \exp\left(-\left[\frac{\mu}{\rho}\right]\right)(\rho t), \tag{1}$$

where I_0 is the incident X-ray beam intensity, I is the transmitted intensity, $[\mu/\rho]$ is the X-ray mass absorption coefficient of the material for the energy of the X-ray beam, t is the (average) thickness of the foil or sample (s) and (ρt) is the integrated column density through the sample of the beam footprint. The beauty of this expression is that the negative values of the natural logarithms of the measured ratios of I/I_0, plotted against t [or (ρt)], fall on a straight line with slope μ (the linear absorption coefficient) or $[\mu/\rho]$. Hence, the mass absorption coefficient, the photoelectric coefficients, the scattering components and the form factors of the material can be directly evaluated from the logarithm of the normalized ratio, and the detector response function on this logarithmic plot should be linear, meaning that the absorption coefficient can be determined from a sample of any thickness. This then gives the input spectrum for extraction of the XAFS, XANES or EXAFS signal and structure.

Equation (1) is deceptively simple in that it assumes that the sample and beam are uniform and the beam intensity can be measured on a zeroed and normalized scale. A simple improvement is to correct for the electronic dark current of the detector D, a correction that is necessary in order for the directly detected detector signal to be linearly related to the absorbance and to normalize the signal to that for a blank measurement b, *i.e.* an absorption measurement with no sample inserted but with a blank or empty foil. This corrects for all attenuation from the air, the windows and the path and ergo defines a more relevant and useful linearity relation,

$$-\ln\left[\frac{\left(\frac{I-D}{I_0-D_0}\right)_{sb}}{\left(\frac{I-D}{I_0-D_0}\right)_{b}}\right] = -\ln\left(\frac{\frac{AYE}{(AYE)_0}\exp[-(\mu t)_{IC1}]\exp[-(\mu t)_{bg}]\exp[-(\mu t)_s]}{\frac{AYE}{(AYE)_0}\exp[-(\mu t)_{IC1}][\exp[-(\mu t)_{bg}]}\right) = \left(\left[\frac{\mu}{\rho}\right](\rho t)\right)_s = (\mu t)_s, \quad (2)$$

where A is the amplification setting of the detector, Y is the electron yield per photon absorbed, E is the detector (ion-chamber) efficiency, D is the dark-current reading, the subscript 0 indicates readings in the upstream (monitor) detector versus the downstream detector, the subscript IC1 indicates the attenuation in the upstream (monitor) detector, the subscript bg indicates the attenuation through the background air path, windows *etc.*, the subscript b indicates measurement of the blank or background signal including attenuation from the air path, windows *etc.* and the subscript sb indicates measurement of the system with the sample of interest included.

Note that this 'simple improvement' demands the measurement of six quantities, $(I)_s$, $(I_0)_s$, $(I)_b$, $(I_0)_b$, D and D_0, rather than two, on the assumption that D, the measurement of electronic noise with the beam off, is time-independent. This also means that in the most simple experiment an estimate of the uncertainty or variance of six quantities is required and that the propagation of uncertainty from raw measurements to an uncertainty in μt requires the evaluation of a 6×6 correlation matrix. Under normal circumstances, uncertainties in D are small and the uncertainty (variance) of the numerator or denominator can be approximated as

$$\sigma^2_{\left[\frac{\mu}{\rho}\right](\rho t)} = \left[\frac{\sigma^2_{\left(\frac{I-D}{I_0-D_0}\right)}}{\left(\frac{I-D}{I_0-D_0}\right)^2} + \frac{\sigma^2_D}{(I-D)^2} + \frac{\sigma^2_{D_0}}{(I_0-D_0)^2}\right]. \quad (3)$$

Fractional or percentage uncertainties (errors) in I/I_0 become absolute uncertainties in the logarithm. We assume here that uncertainties in the overall ratio are decoupled from those of each dark-current measurement. Under almost all operational conditions one should never measure the variance of I and I_0 separately; instead, one directly measures the variance of the corrected ratio. This is explained elsewhere in the literature, and the circumstances where this assumption becomes invalid are also explained (Chantler, Tran, Paterson, Cookson *et al.*, 2000; Chantler, Tran, Paterson, Barnea *et al.*, 2000).

When the full expression of equation (2) is used, with the numerator and denominator combined, with the common assumption that the sample measurement and the blank measurement were made at different times and under different experimental conditions and thus are independent measurements, the resulting variance is given as

$$\sigma^2_{\left(\left[\frac{\mu}{\rho}\right](\rho t)\right)_s} = \left\{\left[\frac{\sigma^2_{\left(\frac{I-D}{I_0-D_0}\right)}}{\left(\frac{I-D}{I_0-D_0}\right)^2}\right]_{sb} + \left[\frac{\sigma^2_{\left(\frac{I-D}{I_0-D_0}\right)}}{\left(\frac{I-D}{I_0-D_0}\right)^2}\right]_{b} + \sigma^2_D\left[\frac{1}{(I_{sb}-D_{sb})} - \frac{1}{(I_b-D_b)}\right]^2 + \sigma^2_{D_0}\left[\frac{1}{(I_{0_{sb}}-D_{0_{sb}})} - \frac{1}{(I_{0_b}-D_{0_b})}\right]^2\right\}. \quad (4)$$

While not complicated, this procedure requires the estimation or determination of four (independent) energy-dependent variances, including a clear strategy for measurement of the blank. This requires careful consideration of the beamline and the measurement of air paths as well as an evaluation of the impact of the variation of physical parameters such as temperature and humidity during the experiment. A schematic of the Australian National Beamline Facility beamline at the Photon Factory is provided in Fig. 1 to illustrate the discussion.

Whenever a sample has a strongly absorbing matrix or is a dilute solution, which is extremely common in XAS and is also

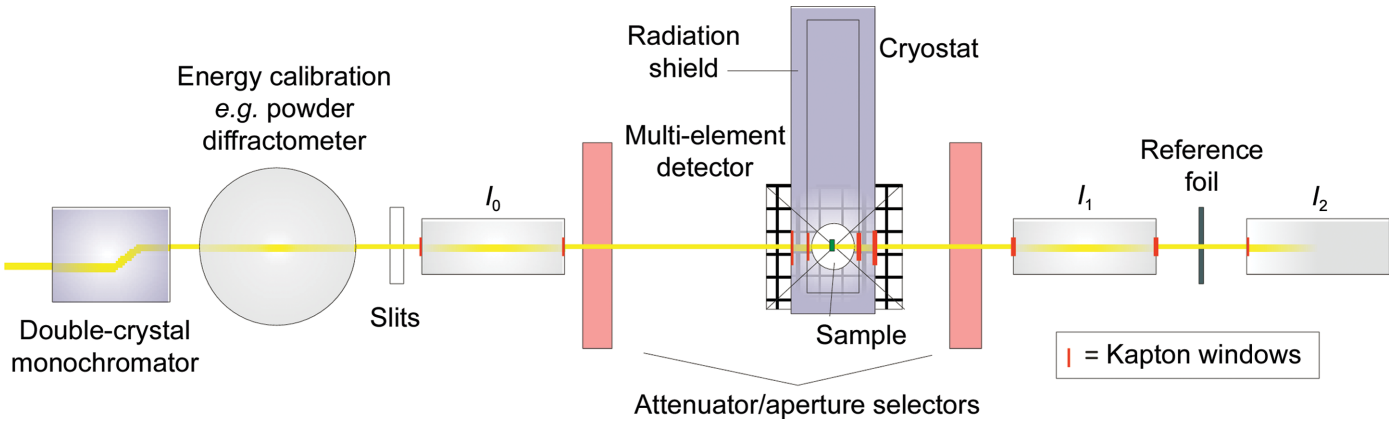

Figure 1
An example of the hybrid technique with simultaneous transmission and fluorescence measurement (Australian National Beamline Facility at the Photon Factory, Tsukuba, Japan). Here I is either I_1 or I_2 in the equations and the reference foil should not be measured simultaneously due to forward and back scattering into the detectors.

one of the primary applications for hybrid measurement, the key XAFS questions will relate to the accuracy and determination of the solute, the active absorber and the surrounding environment. Hence, it is necessary to remove the large background associated with solvent absorption and scattering. This argues strongly for a blank, *i.e.* solvent-only, measurement, implying that the more relevant equation will be

$$\left(\left[\frac{\mu}{\rho}\right](\rho t)\right)_{\rm s} = -\ln\left[\frac{\left(\frac{I-D}{I_0-D_0}\right)_{\rm sb}}{\left(\frac{I-D}{I_0-D_0}\right)_{\rm b}}\right] = -\ln\left[\frac{\left(\frac{I-D}{I_0-D_0}\right)_{\rm S+SV+BKG}}{\left(\frac{I-D}{I_0-D_0}\right)_{\rm SV+BKG}}\right] \quad (5)$$

This formulation of equation (2) requires the sample (s) to be interpreted as the solute (S) and the background (b) to include contributions from the solvent (SV) and the background (BKG). This still represents two independent measurements, so the uncertainty could again be given by equation (4). Under normal circumstances the path length and density of the solute and solvent is not identical to that of the solvent. However, the background components from the air path, windows *etc.* might hopefully be identical, so it is useful and important to separate the BKG component from the SV component. This can be performed either by a separate measurement of an empty cell (a true blank BKG) or by measurement of the geometry of the beamline to the detector. Additionally, the effective path-length ratio $t_{\rm ratio}$ for the sample-cell thickness t to that of the solvent-cell measurement $t_{\rm SV}$ can be fitted to allow for known variations in density or cell path length. In this common case the functional equation becomes

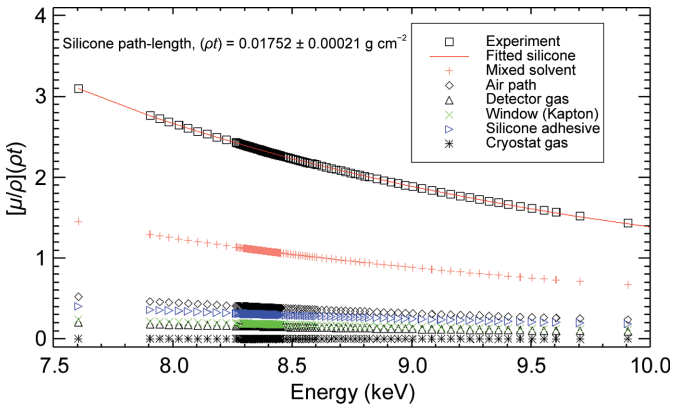

Figure 2
Example evaluation of background and uncertainty following equation (8). The path length of two layers of silicone adhesive used on the Kapton windows was fitted, while the attenuations of all other identified absorbers were in good agreement with their estimated values. An excellent fit was obtained for the solvent path length required to determine the accuracy of the XAS from the solutions. Interestingly, despite all being represented by smooth and largely featureless curves, the analysis could easily distinguish between errors of one component of the background path compared with another because the slopes and curvatures are significantly different.

$$\begin{aligned}\left(\left[\frac{\mu}{\rho}\right](\rho t)\right)_{\rm s} &= (\mu t)_{\rm s} \\ &= -\ln\left(\frac{I-D}{I_0-D_0}\right)_{\rm S+SV+BKG} + \frac{t}{t_{\rm SV}}\ln\left(\frac{I-D}{I_0-D_0}\right)_{\rm SV} \\ &\quad + \ln\left(\frac{I-D}{I_0-D_0}\right)_{\rm BKG} \\ &= -\ln\left(\frac{I-D}{I_0-D_0}\right)_{\rm S+SV+BKG} + t_{\rm ratio}\ln\left(\frac{I-D}{I_0-D_0}\right)_{\rm SV} \\ &\quad - \left(\left[\frac{\mu}{\rho}\right](\rho t)\right)_{\rm BKG}. \end{aligned} \quad (6)$$

If the sample (S+SV+BKG) and solvent (SV+BKG) are then measured, the background from windows, air path *etc.* is measured or calculated and the effective path-length ratio is measured, estimated or fitted, then the uncertainty will propagate as

$$\begin{aligned}\sigma^2_{\left(\left[\frac{\mu}{\rho}\right](\rho t)\right)_{\rm s}} &= \left\{\left[\frac{\sigma^2_{\left(\frac{I-D}{I_0-D_0}\right)}}{\left(\frac{I-D}{I_0-D_0}\right)^2}\right]_{\rm S+SV+BKG} + \left[\frac{\sigma^2_{\left(\frac{I-D}{I_0-D_0}\right)}}{\left(\frac{I-D}{I_0-D_0}\right)^2}\right]_{\rm SV+BKG}\right. \\ &\quad + \sigma^2_{\left(\left[\frac{\mu}{\rho}\right](\rho t)\right)_{\rm BKG}} + \sigma^2_{t_{\rm ratio}}\ln^2\left(\frac{I-D}{I_0-D_0}\right)_{\rm SV} \\ &\quad + \sigma^2_D\left[\frac{1}{(I_{\rm sb}-D_{\rm sb})} - \frac{1}{(I_{\rm b}-D_{\rm b})}\right]^2 \\ &\quad \left. + \sigma^2_{D_0}\left[\frac{1}{(I_{0_{\rm sb}}-D_{0_{\rm sb}})} - \frac{1}{(I_{0_{\rm b}}-D_{0_{\rm b}})}\right]^2\right\}. \end{aligned} \quad (7)$$

An example of the energy-dependent attenuation from the component absorbers for the beamline shown in Fig. 1 is given in Fig. 2. See the error analysis in Chantler *et al.* (2015).

For dilute samples the background subtraction can be made experimentally with correction for a different cell length, window and position, and a good estimate can be made from very careful beamline measurements followed by theoretical modelling. In general, any such beamline measurements following equation (8) need only be performed once for each configuration. An example of the implementation of this approach is given for hybrid technique measurements applied to 1.5 mM frozen solutions of nickel(II) coordination complexes (Section 6; Chantler *et al.*, 2015),

$$\begin{aligned}-\ln\left(\frac{I-D}{I_0-D_0}\right)_{\rm SV+BKG} &= \left(\left[\frac{\mu}{\rho}\right](\rho t)\right)_{\rm SV} + \left(\left[\frac{\mu}{\rho}\right](\rho t)\right)_{\rm air\ path} \\ &\quad + \left(\left[\frac{\mu}{\rho}\right](\rho t)\right)_{\rm windows} \\ &\quad + \left(\left[\frac{\mu}{\rho}\right](\rho t)\right)_{\rm upstream\ ion\ chamber\ gas} \\ &\quad + \left(\left[\frac{\mu}{\rho}\right](\rho t)\right)_{\rm cryostat\ gas}. \end{aligned} \quad (8)$$

Notice that many nonlinearities in the detection chain are addressed by these equations when applied to transmission experiments. Scattering (see Chantler, 2024; Bridges, 2024*b*; Ciatto *et al.*, 2024; de Jonge *et al.*, 2004*a*; Tran, Chantler *et al.*,

2004), sample impurities (d'Acapito, 2024; Glover *et al.*, 2010), harmonics (Tran, Barnea *et al.*, 2003; Barnea *et al.*, 2011) and bandwidth (Bunker, 2024*b*; de Jonge *et al.*, 2005) should also be allowed for and corrected where appropriate, together with the effects of sample roughness (Chantler, Tran, Paterson, Barnea *et al.*, 2000) and integrated column density variation (Chantler, 2001; Tran, de Jonge *et al.*, 2004). Mismatched detectors or even mismatched ion chambers (gas type, flow rate, chamber length and construction) can lead to scale errors and energy-dependent errors, and the reader is invited to follow those experimental issues in related chapters of this volume. Determination of the absolute absorption coefficient is usually not expected for XAS measurements unless it is to be used in calibration and definition of primary or secondary experimental standards or references. Determining a local beam-dependent average thickness requires careful mapping, which is usually appropriate for well defined homogeneous solid samples such as metals and single crystals, and the small absolute uncertainty for solutions and liquids is usually quite challenging to measure. Since the results are used in structural modelling in XAFS, such scaling errors can yield uncertainty in the modelled amplitude factors of the XAFS equation.

4. Coupled beam structure and sample non-uniformity

Any detector measurement is a proper pointwise integral over all variation, spatial x, y, energy and angular, and hence momentum vector $\mathbf{k}$, temporal t and polarization ε, including any sample inhomogeneity across the beam path. If we neglect the corrections to detector, background, linearity and path, and correlations of measurement, represented by equations (2)–(8), then in terms of the two signals I_1 and I_0 entering each detector, instead of equation (1), we should consider more broadly

$$\left[\frac{I_0(E_{\rm mono})}{I_1(E_{\rm mono})}\right] = \frac{\iiint_{x,y,\mathbf{k},\varepsilon,t}^{\rm monitor} I_{00}(E_{\rm mono},x,y,\mathbf{k},\varepsilon,t)\,{\rm d}x\,{\rm d}y\,{\rm d}t\,{\rm d}\mathbf{k}\,{\rm d}\varepsilon}{\iiint_{x',y',\mathbf{k}',\varepsilon',t'}^{\rm detector} I_{00}(E_{\rm mono},x',y',\mathbf{k}',\varepsilon',t')\,{\rm d}x'\,{\rm d}y'\,{\rm d}t'\,{\rm d}\mathbf{k}'\,{\rm d}\varepsilon'}. \quad (9)$$

Ideally, each element or ray component in the integral over the photon flux at a given monochromator energy, after correction for blank, path *etc.*, can be represented by a modified version of equation (1),

$$I_{10}(E_{\rm mono},x',y',\mathbf{k}',\varepsilon,t',T) = I_{00}(E_{\rm mono},x,y,\mathbf{k},\varepsilon,t) \times \exp\left(-\left[\frac{\mu}{\rho}\right]_T \{\rho z(x,y)/\cos[\theta(x,y,\mathbf{k})]\}\right). \quad (10)$$

These multidimensional integrals are all coupled and hence are not representable as convolutions. However, convolution approximations usually work very well, and often this coupling and hence the correlation is sparse and separable, as explained above. Sample inhomogeneities include thickness variations, for example tapering, wedges, pinholes, cracks or nano-roughness, as well as sample impurities and inhomogeneity in general, which are all generally represented in the x, y, z terms. Harmonics and bandwidth are represented in the dependence upon $\mathbf{k}$. Divergence is represented by the vector nature of $\mathbf{k}$ and by θ. Any beam structure is represented by the functional of I_{00} and indeed the polarization as a function of this on-axis or off-axis. Temporal instability of the position, angle and structure of the beam is represented by time t; indeed, small variations, for example due to the footprint on the monochromator or mirror, produce potentially repeatable noise-like structure as a function of energy. Such details can limit the data quality, but they can also be quantified. In any arbitrary experiment different effects may dominate; these generally fall into well defined types as now discussed. Changes in the temperature T of any component in the path change the density and thermal broadening. Additionally, changes in the sample temperature change the local structure, bond lengths and dynamic parameters.

If not characterized and normalized, the combination of sample variations and beamline structure leads to variations in the ratio I_0/I_1 that can look like repeatable noise for some energy ranges and produce significant amplitude variations at monochromator glitches. Cryostat windows are usually curved so the effective window thickness varies slightly if the cryostat is translated. Important changes can occur if a focused beamline is used or if the beam position drifts with time or energy. Therefore, one should measure a blank at each energy to normalize out window and beam variation and most temporal variation, as discussed above and below. One should investigate and characterize the bandwidth and energy dependence (harmonics, Chantler, 2000; Section 5.1; bandwidth, Glover & Chantler, 2009; Section 5.2), which to first order separates the convolution of these with any sample homogeneity or XAS structure. Ideally, sample profile, inhomogeneity and non-uniformity should be mapped and characterized (Section 5.5), and in this sense separates the sample dependence from the beam structure (Diaz-Moreno & Strange, 2018; Pease, 1976; Koningsberger & Prins, 1988; Krappe & Rossner, 1999; Tran, Barnea *et al.*, 2003; Pettifer *et al.*, 2005; Bunker, 2010). Measurements of nano-roughness (Section 5.5) can be performed using nondestructive X-ray techniques for investigating this within the structure of the beam, fully independently of an XFM or sample-mapping technique (Barnea *et al.*, 2011; Tantau *et al.*, 2015). It is more challenging to isolate the impact of nano-roughness further, although studies have been reported (Li *et al.*, 1994; Sutter *et al.*, 2016) and are discussed elsewhere (see Diaz-Moreno & Boada, 2022; Suzuki, 2024; Bridges, 2024*a*; Lawniczak-Jablonska, 2024; Bunker, 2024*b*; De Panfilis & Bardelli, 2024; Ciatto *et al.*, 2024; d'Acapito, 2024).

Temperature variations of the sample and beamline endstation can introduce a range of systematic errors. The experiment design needs to ensure that the sample temperature is equilibrated before the start of measurements and is recorded during the acquisition of spectra.

5. Identification and correction of systematic errors impacting on fluorescence-detected XAS measurements

Several quite independent systematics are commonly grouped under the heading of 'thickness effects'. These have different

signatures in terms of the distortions that they produce and the reproducibility of the measurements. Sections 5.1–5.4 relate to effects on the spectrum due to the finite thickness of the sample, Section 5.5 relates to the effect of variations in thickness, density or composition across the sample, Section 5.6 relates to the dominant effects of this in fluorescence, namely absorption and self-absorption, and Section 5.7 briefly discusses the impact of different processing methodologies for fitting (XAFS) structure.

5.1. Beam harmonic energy composition (contamination)

Beam harmonic energy composition (contamination) leads to nonlinear changes in the apparent absorption coefficient with thickness. This affects the monitor signal in both transmission and fluorescence experiments. Often, the monochromator design dictates that the third harmonic is the dominant contamination, but this can vary. The second harmonic, while forbidden for many monochromator reflections, can be present. Clearly, this would affect the monitor signal in both transmission and fluorescence experiments. The fluorescence detector usually sets a region of interest (ROI) to exclude this effect in the detector, but also causes a systematic error in the coefficient due to the upstream signal. Hence, measurements with different thicknesses of a flat homogeneous sample will yield different attenuation coefficients. In transmission this can lead to a damping of the oscillations (with increasing harmonic or thickness; Lu *et al.*, 1989; Ovsyannikov & Shuvaev, 1995), while in fluorescence it will tend to lead to a loss of efficiency and hence measured coefficient, although this thickness effect will saturate towards higher thicknesses. At lower energies a harmonic rejection mirror can be very effective, but a level of harmonics after the rejection mirror is often present but not calibrated. The harmonics usually have a lower attenuation coefficient, usually with no XAFS structure or edge, so under these circumstances the harmonic contamination adds an energy-dependent background function to the spectrum, and in general the oscillations are therefore effectively damped. For a single harmonic in transmission, the relation is given by

$$\frac{\left(\frac{I-D}{I_0-D_0}\right)_{\rm sb}}{\left(\frac{I-D}{I_0-D_0}\right)_{\rm b}} = (1-\alpha)\exp\left\{-\left(\left[\frac{\mu}{\rho}\right](\rho t)\right)\right\}_{\rm f} + \alpha\exp\left\{-\left(\left[\frac{\mu}{\rho}\right](\rho t)\right)\right\}_{\rm h}, \quad (11)$$

where α is the effective harmonic fraction and $[\mu/\rho]_{\rm f}$ and $[\mu/\rho]_{\rm h}$ are the attenuation coefficients at the fundamental energy (usually that being investigated) and at the energy of the harmonic contamination, respectively. Under some circumstances an extremely thin sample limit can be used to minimize the impact of harmonics, although this depends upon a small α and high attenuation for the fundamental. The harmonic coefficient can often be represented to high accuracy by theoretical tables (Chantler, 1995, 2000) to enable clear quantification of α and extraction of the true attenuation coefficient from the data. This is most easily computed and corrected using multiple samples of a reference foil (Glover & Chantler, 2009) or a material such as aluminium (Tran, Barnea *et al.*, 2003) that likewise probes the functional of the harmonic spectrum. Uncertainties in α can be below 0.01%. In fluorescence, with multipixel detectors or otherwise, the harmonic frequencies will not fall within the ROI and an apparent attenuated fluorescence yield will result.

5.2. Synchrotron beam bandwidth

Bandwidth is defined as the spread of energies across the upstream X-ray beam entering the monitor detector. Transmission and fluorescence spectra of a sample recorded using sources with different bandwidths will exhibit differences in the edge location and the resolution, with thickness-dependent differences in attenuation coefficients and the apparent edge structure (Parratt *et al.*, 1957; Pease, 1976). Bandwidth effects can have an arbitrary functional form, especially, for example, off-axis. A general expression for the broadening of the spectrum is given as (Hayakawa *et al.*, 1991)

$$\exp\left(-\left[\frac{\mu}{\rho}\right]_{{\rm m}E_{\rm mono}}(\rho t)\right) = \frac{\int_0^\infty I(E)\,{\rm d}E}{\int_0^\infty I_0(E)\,{\rm d}E}, \quad (12)$$

where the relation between each component I is given above and m is the measured value of the central energy of the distribution function given by $E_{\rm mono}$. Compared with the value obtained for a single energy component (the 'true' value $[\mu/\rho]_{{\rm t}E_{\rm mono}}$), the correction of the measured attenuation coefficient, say across an edge, in a linear regime (de Jonge *et al.*, 2004*b*; Tantau *et al.*, 2015; Glover & Chantler, 2009) can be given or approximated by

$$\begin{aligned}\Delta\left[\frac{\mu}{\rho}\right]_{E_{\rm mono}} &= \left[\frac{\mu}{\rho}\right]_{{\rm t}E_{\rm mono}} - \left[\frac{\mu}{\rho}\right]_{{\rm m}E_{\rm mono}} \\ &\simeq \frac{1}{\rho t}\ln\left[\frac{1}{\int_0^\infty I_0(E)\,{\rm d}E}\int_0^\infty I_0(E) \right. \\ &\quad \left. \times \exp\left\{-\frac{{\rm d}\left[\frac{\mu}{\rho}\right]_{{\rm t}E_{\rm mono}}}{{\rm d}E}(E-E_{\rm mono})\rho t\right\}{\rm d}E\right]. \quad (13)\end{aligned}$$

The functional form can be deduced from multiple thickness measurements, although the effect does not disappear in the limit of zero thickness. If the distribution is approximately Gaussian or truncated Gaussian with a given FWHM, then the second-order approximation of equation (14) is compact and valid across a broader range, allowing the efficient extraction of the ideal edge profile with higher resolution (Tantau *et al.*, 2015),

$$\begin{aligned}\Delta\left[\frac{\mu}{\rho}\right]_{E_{\rm mono}} &= \left[\frac{\mu}{\rho}\right]_{{\rm t}E_{\rm mono}} - \left[\frac{\mu}{\rho}\right]_{{\rm m}E_{\rm mono}} \\ &\simeq \frac{\sigma^2}{2}\left\{\left[\frac{\mu}{\rho}\right]'^2_{{\rm t}E_{\rm mono}}(\rho t) - \left[\frac{\mu}{\rho}\right]''_{{\rm t}E_{\rm mono}}\right\}. \quad (14)\end{aligned}$$

5.3. Monochromator 'glitches': secondary Bragg diffraction peaks

Monochromator glitches (secondary Bragg diffraction peaks) primarily yield a change in incident intensity and secondarily in energy. The intensity variation should be fully corrected for in transmission if the detectors are perfectly linear, in turn requiring valid dead-time correction and avoidance of saturation (Diaz-Moreno & Strange, 2018; Pease, 1976; Koningsberger & Prins, 1988; Krappe & Rossner, 1999; Tran, Barnea *et al.*, 2003; Pettifer *et al.*, 2005; Bunker, 2010). Such glitches have been documented by beamline scientists for a particular monocrystal at a particular beam position, for example on the Diamond Light Source beamlines (Diaz-Moreno, 2012; Sutter *et al.*, 2016; Diaz-Moreno & Strange, 2018). However, such glitches in general are large and dispersive. The upstream (monitor) detector and the downstream transmission detector are usually matched in attenuation and gas type, so these changes in efficiencies normalize using XERT (de Jonge *et al.*, 2004*a*, 2005; Tran, Chantler *et al.*, 2004; Chantler, 2009; Glover *et al.*, 2010; Rae *et al.*, 2010; Chantler, Barnea *et al.*, 2012; Tantau *et al.*, 2014; Chantler *et al.*, 2015). However, in fluorescence the changes in efficiency and linearity (with energy or flux, for example, towards dead-time corrections and saturation) do not in general match those of the monitor, so we usually observe that glitches in transmission normalize out (for example using XERT), while glitches in fluorescence remain in the data (Trevorah *et al.*, 2019) and most users delete these points (see Sutter, 2024; Ciatto *et al.*, 2024).

Bragg diffraction peaks will also arise from the sample, whether due to low-temperature frozen-sample crystallization of solvent or oriented crystalline samples such as perfect silicon. In this case these 'Bragg glitches' can destroy the value of the data for XAFS investigation, but they can be uniquely identified from the multiple samples with small changes of orientation and dealt with accordingly (de Jonge *et al.*, 2004*a*, 2005; Tran, Chantler *et al.*, 2004; Chantler, 2009; Glover *et al.*, 2010; Rae *et al.*, 2010; Chantler, Barnea *et al.*, 2012; Tantau *et al.*, 2014; Chantler *et al.*, 2015).

5.4. Synchrotron beam spatial structure

The spatial beam structure may exhibit non-uniformity and divergence or convergence in both horizontal and vertical axes, leading to distortion of the spectra of heterogeneous or structured (variable-thickness) samples. In both transmission and fluorescence measurements this yields an averaging or broadening of the spectrum. In a flat uniform sample, the spatial (x, y) beam structure cancels in transmission, while the fluorescence signature can lead to a broadening due to the consequential angular dependence. The angular structure of the beam (divergence or convergence in θ_x and θ_y and non-uniformity) can lead to broadening and distortion of the spectrum even for a uniform homogeneous sample in both transmission and fluorescence.

5.5. Sample inhomogeneities (pinholes, cracks, voids, bubbles, grains, roughness and thickness variations)

Any deviation of the sample from a perfect flat plate, and any variation of thickness or impurity or composition across the beam profile, will yield a different value for the mass absorption coefficient from the sample. These 'thickness' effects depend upon the variation of sample thickness or orientation in the beam as opposed to the 'thickness effects' discussed in Sections 5.1–5.4, which are due to the beam distribution and profile and would exist for any sample thickness. Most extreme are non-light-tight samples with pinholes or micro-cracks, but this effect can arise from samples in the form of a perfect wedge, a curved surface or thickness profile, or any variation of the integrated column density thickness or composition (Stern & Kim, 1981; Babanov *et al.*, 2001). The most general form of this is a definition of the roughness of the sample. Both transmission and fluorescence spectra are affected and distorted and may be rendered unusable unless there is minimal relative movement of the X-ray beam and sample during the measurement and there is no energy-dependent change in the spatial beam structure.

Any homogeneous sample will have nonuniformities of the sample thickness on the nanoscale which can be characterized by mapping the absorption coefficient over an area of the sample. In XERT, thickness mapping is used to define an absolute attenuation compared with the point of the sample through which the X-ray beam passes, compared with the average thickness determined separately (Rae *et al.*, 2010). Roughness in transmission then represents the moments of the integrated column density functional within the beam footprint through the sample. Measurement of the roughness of the sample under the beam can explain the nature of the sample origin, for example, from crystal growth, from tooling, from a local wedge and other patterns. We define roughness as the variability in (ρt), the integrated column density, seen by the X-ray beam passing through the sample (Chantler, Tran, Paterson, Cookson *et al.*, 2000),

$$(\rho t) = \int_P \rho(x)\,\mathrm{d}x, \tag{15}$$

where P is the path of the X-ray beam and $\rho(x)$ is the density of the sample at point x. We define the magnitude of the roughness of a sample (in the region of the X-ray beam) using the variance of the integrated column density given by

$$\sigma^2_{(\rho t)} = \frac{1}{A}\int\int_{S(x,y)} [(\rho t)_{(x,y)} - (\rho t)_{\mathrm{ave}}]^2\,\mathrm{d}S, \tag{16}$$

where S corresponds to the region of the sample being illuminated with area A, assuming that the foil sample is oriented normal to the beam. Then, assuming uniform incident intensity across the beam profile (see above), the roughness changes the measured mass attenuation coefficient,

$$\exp\left(-\left[\frac{\mu}{\rho}\right]_{\mathrm{m}}(\rho t)\right) = \frac{1}{A}\int\int_{S(x,y)} \exp\left(-\left[\frac{\mu}{\rho}\right](\rho t)_{(x,y)}\right)\mathrm{d}S, \tag{17}$$

from which the change of the measured mass attenuation coefficient from that of a perfectly flat surface is given by

$$\Delta\left[\frac{\mu}{\rho}\right] = \frac{-1}{(\rho t)_{\rm ave}} \ln\left(1 - \frac{\left[\frac{\mu}{\rho}\right]_{\rm m}^2 \sigma^2_{(\rho t)}}{2}\right). \qquad (18)$$

Hence, the measurement of attenuation coefficients relative to a smooth reference foil will yield a measurement of, and a correction for, nano-roughness which has a clear dependence on the mass attenuation coefficient.

Because two angles are involved, the impact of roughness on fluorescence measurements is more complicated than that for the transmission case, and indeed is much more significant for any of the grazing- or normal-incidence geometries in which the incident or outgoing angles are small. However, in conventional (45°) fluorescence measurements roughness *per se* may be a minor systematic, particularly for solution cells, which will often have smooth (flat or curved) windows. While curved windows give a sample position-dependent non-uniform background and can be different for the blank sample, a blank measurement is generally sufficient to address the large first-order effect of this correction. Of course, this consideration is sample-dependent.

5.6. Absorption and self-absorption

The primary beam is absorbed and attenuated as a function of thickness or penetration depth. In transmission, the attenuated beam gives the mass attenuation coefficient from the measurement and can be corrected to give the mass absorption coefficient by removing the (nonlinear) contribution to attenuation from scattering if known or measured; if not, this contributes a general background loss function due to scattering, *i.e.* to attenuation versus absorption, and to deviations from the Beer–Lambert relation. Corrections for these effects are straightforward based on measurements from samples of different thickness. In transmission there is often a significant fluorescence signal of characteristic radiation relating to the absorption edge involved; this can be corrected for using different calibrated apertures. However, in fluorescent detection this lower energy photon is the primary detected event in the fluorescence detector, and there will be self-absorption (self-attenuation) as the fluorescent photons are created in the sample and propagate towards the detector. Fluorescence measurements present significant complications owing to the geometry dependence of the path length for the incident and fluorescent photons (Tan *et al.*, 1989; Hayakawa *et al.*, 1991; Tröger *et al.*, 1992; Iida & Noma, 1993; Meitzner & Fischer, 2002). The impact of this systematic is especially obvious in multi-pixel detection in fluorescence measurements, where self-absorption is responsible for the dominant angular dependence of the spectra from each pixel.

Fluorescence measurement, which was developed as a particularly valuable approach for dilute systems in the 1970s and 1980s (Lee *et al.*, 1981; Jaklevic *et al.*, 1977, 1993; Pease *et al.*, 1989), has since become the technique of choice for most XAS studies, but suffers from detector nonlinearities, dead-time correction, ROI issues and sample-thickness effects (Goulon *et al.*, 1982). It has also spawned such techniques as resonant inelastic X-ray scattering (RIXS), as described in Glatzel *et al.* (2024). Individual pixels will have individual dead-time corrections and individual amplification and this should generally have been calibrated at the beginning of the experiment or during pre-processing (see De Panfilis & Bardelli, 2024). Fluorescence measurements present significant complications owing to the geometry dependence of the path length of the incident and fluorescent photons (Tan *et al.*, 1989; Hayakawa *et al.*, 1991; Tröger *et al.*, 1992; Iida & Noma, 1993; Meitzner & Fischer, 2002). The impact of this systematic is especially obvious in multi-pixel detection in fluorescence measurements, where self-absorption is responsible for the dominant angular dependence of the spectra from each pixel. After early work on this using a known stoichiometry (Goulon *et al.*, 1982; Tröger *et al.*, 1992), multiple measurements at different detection angles (Eisebitt *et al.*, 1993) or known energy dependence of absorption coefficients (Pfalzer *et al.*, 1999), general approaches have been investigated (Booth & Bridges, 2005; Chantler, Rae *et al.*, 2012; Trevorah *et al.*, 2019).

The core equation for a fluorescence-detected measurement is given as (Jaklevic *et al.*, 1977; Pease *et al.*, 1989; Trevorah *et al.*, 2019; Booth & Bridges, 2005; Chantler, Rae *et al.*, 2012)

$$I_{\rm f} = \frac{f I_0 \Omega [\mu/\rho]^*_{\rm pe}/(4\pi \cos\theta_{\rm inc})}{[\mu/\rho]/(\cos\theta_{\rm inc}) + (\mu_{\rm f}/\rho)/(\cos\theta_{\rm out})} \times \left\{1 - \exp\left[-\frac{[\mu/\rho](\rho t)}{\cos\theta_{\rm inc}} - \frac{[\mu_{\rm f}/\rho](\rho t)}{\cos\theta_{\rm out}}\right]\right\}, \qquad (19)$$

where $I_{\rm f}$ is the number of fluorescent photons emitted from the surface of the material, the asterisk indicates that only the component absorbed in the absorber producing a fluorescent photon is relevant, 'pe' signifies that only the photoelectric component can yield a fluorescent photon, Ω represents the solid angle subtended by each detector pixel, $\theta_{\rm inc}$ is the incident angle of the X-rays onto the sample, $\theta_{\rm out}$ is the emission angle of the fluorescent X-rays from the sample and $[\mu_{\rm f}/\rho]$ is the mass attenuation coefficient of the material at the energy of the fluorescent photon. Because this functional depends upon the path length and angle, it also depends upon any thickness inhomogeneity and the angle of alignment of both the sample and the detector (pixel) location. It is assumed that this formula is corrected for dark current at least in the upstream detector, and it is assumed that any ROI (region of interest) set includes all of these photons and excludes any photons from different processes which might overlap in energy and space. To consider the number of detected measured photons, we in general consider the functional for the energy-dependent factors (upstream, A, for absorption corrections) as given in equation (20). Note that the ROI may overlap with the elastic peak tail, which can complicate the analysis further.

$$\left[\frac{I_f}{I_{0\,\mathrm{monitor}}}\right]_A = \frac{I_f}{I_0}\left[\frac{1}{\varepsilon_{\mathrm{mon}}(E)}\right]_A\left[\frac{\varepsilon_{\mathrm{det}}(E)}{\varepsilon_{\mathrm{mon}}(E)}\right] \times \exp\left\{-\left[\frac{\{[\mu/\rho](\rho t)\}_{\mathrm{air}}}{\cos\theta_{\mathrm{air}}}\right]_A - \left[\frac{\{[\mu/\rho](\rho t)\}_{\mathrm{w}}}{\cos\theta_{\mathrm{w}}}\right]_A \times \left[\frac{\{[\mu/\rho](\rho t)\}_{\mathrm{m}}}{\cos\theta_{\mathrm{m}}}\right]_A\left[\frac{\{[\mu/\rho](\rho t)\}_{\mathrm{c}}}{\cos\theta_{\mathrm{c}}}\right]_A\right\}, \quad (20)$$

where $\varepsilon_{\mathrm{det}}$ and $\varepsilon_{\mathrm{mon}}$ represent the energy-dependent detector quantum efficiency, $t_{\mathrm{air}}/\cos\theta_{\mathrm{air}}$ is the path length of the photons from the monitor to the front surface of the sample, and similarly for any window materials w, the monitor gas path m and the cryostat or other gas path c. Curvature of the Kapton windows at the air–vacuum interface of the cryostat has been treated as a minor perturbation. Additives such as silicone adhesive are included in the calculation of $[\mu/\rho]_{\mathrm{w}}$. The $[\mu/\rho]$ X-ray mass absorption coefficient of each component material is energy-dependent. For the fluorescent photons emitted from the surface and measured using a multi-pixel detector, a second functional is required,

$$\left[\frac{I_f}{I_{0\,\mathrm{monitor}}}\right]_F = \left[\frac{I_f}{I_{0\,\mathrm{monitor}}}\right]_A[\varepsilon_{\mathrm{det}}(E)]_F - \exp\left\{\left[\frac{\{[\mu_f/\rho]\}(\rho t)\}_{\mathrm{air}}}{\cos\theta_{\mathrm{air}}}\right]_F - \left[\frac{\{[\mu_f/\rho](\rho t)\}_{\mathrm{w}}}{\cos\theta_{\mathrm{w}}}\right]_F - \left[\frac{\{[\mu_f/\rho](\rho t)\}_{\mathrm{m}}}{\cos\theta_{\mathrm{m}}}\right]_F - \left[\frac{\{[\mu_f/\rho](\rho t)\}_{\mathrm{c}}}{\cos\theta_{\mathrm{c}}}\right]_F\right\}, \quad (21)$$

where all symbols have their previous meaning except that F, downstream, self-absorption corrections, describes the path lengths from the sample to the detected photon at a particular pixel and the fluorescent photons must use attenuation coefficients for the fluorescent photon $[\mu/\rho]_f$. Since the energy of each fluorescent photon is not dependent upon the incident energy, these factors are not energy-dependent but they are geometry-dependent, *i.e.* angle-dependent and pixel-dependent. Numerous sources give idealized simplifications of a very thin, concentrated solution limit and a thick, dilute solution limit which, however, hide the significant nonlinearities of most real spectra. It is also important to recognize the formal lack of an inversion formula, which however has been addressed, for example, in the *SeAFFlux* package (Trevorah *et al.*, 2019). In particular, as soon as one sees the fluorescent spectra diverging for different pixels away from the edge, or increasing with energy or k above the edge, one knows that the nonlinearities and 'thickness effects' are dominant. Nonlinearities include X-ray scattering and X-ray Raman scattering (Glatzel *et al.*, 2024), including matrix effects (Bunker, 2024*a*; Heald, 2024; d'Acapito, 2024), and the positive slope should be extracted in order to achieve a linear response, which is then interpretable as an absorption or attenuation coefficient (Trevorah *et al.*, 2019). Analytic and computational estimates of the correction for this in the mass absorption coefficient and hence in the XAFS functional are treated in detail elsewhere (Trevorah *et al.*, 2019).

5.7. *k* versus *r* processing

Particular experimental systematic errors may invite double transforms with filtering, which is discussed and commended by Bunker (2024*c*) and Newville (2024).

Fits in either k-space or r-space must look at all paths within the range. It is certainly necessary to consider outer shells and multiple paths, but this can be performed intelligently in k-space. In r-space the FT limitations, offsets and images of lower paths increase the systematics, make the analysis more complex and problematic, and certainly decrease the information content, especially when there are no propagated error bars. Further, in r-space it is common to 'clean' the transform with low and high filters, which both destroys data and introduces artefacts. In k-space the real data are used directly (see Bunker, 2024*c*,*d*; Liu & Frenkel, 2024; Kavčič & Žitnik, 2024; Newville, 2024).

6. Case studies

The limited number of studies so far published which satisfy the hybrid criteria of high and defined point-by-point accuracy have been concerned with the distinction between geometric isomers. In such cases the single-scattering paths are identical, and the multiple-scattering paths provide a distinction between the EXAFS of the isomeric forms. In these cases, distinction between models based on the alternate geometries are subtle and robust statistical analysis is needed to provide an assessment of the reliability of the conclusions drawn from the analysis.

6.1. Tetrahedral/square-planar distortion of four-coordinate complexes

For later first-row transition metals the relative energies of square-planar (D_{4h}) and tetrahedral geometries of four-coordinate complexes can be finely balanced, and this can impact on the chemistry and catalysis of these metal ions in chemical and biological environments. Distortions from the limiting high-symmetry geometry will depend both on intramolecular and intermolecular interactions, and EXAFS can play an important role in establishing the geometry in cases where crystalline diffraction cannot be used to solve the structure, for example for complexes in disordered environments.

The differing geometries of four-coordinate metal complexes reflect an electronic preference for the D_{4h} form for particular d-electron counts (for example d^8) and the minimization of ligand–ligand repulsion by the adoption of tetrahedral geometry. A good example of this effect is provided by the *N*-propylsalicylaldiminato complexes of nickel(II), which give neutral compounds with N_2O_2 coordination of the metal (Sacconi, 1966; Fox *et al.*, 1963; Holm & Swaminathan, 1963). The geometry of the compound can be tuned by steric effects associated with the *N*-alkyl group. In the solid state, the *n*-propyl compound (Ni-^{n}Pr-Sal) has an approximately planar geometry, while the more sterically demanding *i*-propyl form (Ni-^{i}Pr-Sal) has distorted tetrahedral coordination (Fox *et al.*,

1964; Britton & Pignolet, 1989; Fig. 3). The difference in geometry is reflected by their spectroscopic and magnetic properties (planar and diamagnetic or tetrahedral and paramagnetic) and impacts on chemical properties such as their tendency to form dimers (Benelli *et al.*, 1972; Hill *et al.*, 1973; Knorr *et al.*, 2007). Molecular-weight determination for the solution species suggests that the monomeric species dominates (Sacconi *et al.*, 1964). The temperature dependence of the magnetization has been interpreted in terms of square planar–tetrahedral isomerism, in which the complexes with a secondary C atom bound to the N atom (Ni-^{i}Pr-Sal) yield predominantly tetrahedral coordination, particularly for solutions at higher temperatures (Sacconi *et al.*, 1963, 1964; Sacconi, 1966).

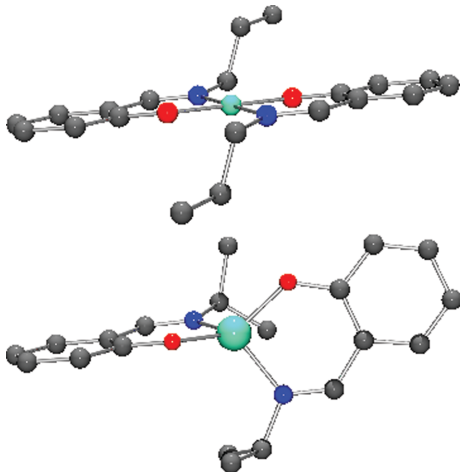

Figure 3
X-ray structures of bis(*N*-propylsalicylaldiminato)nickel(II) (Ni-^{n}Pr-Sal; Britton & Pignolet, 1989) and bis(*N*-isopropylsalicylaldiminato)nickel(II) (Ni-^{i}Pr-Sal; Fox *et al.*, 1964). For clarity, H atoms are omitted.

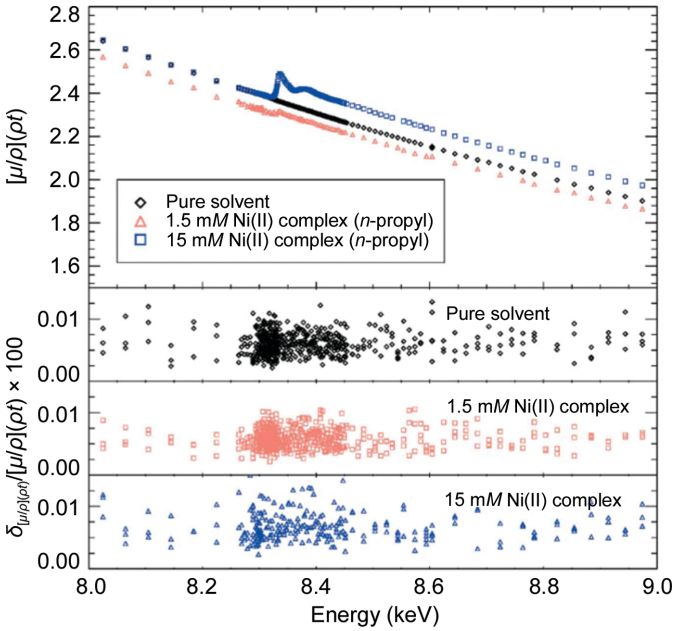

Figure 4
X-ray absorption spectra using two solutions (15 and 1.5 m*M*) of Ni-^{n}Pr-Sal and the acetonitrile/butyronitrile mixed solvent together with determination of their corresponding uncertainty or the independent quality of the data. Past conventions would reject these absorption data on the basis of poor signal-to-background ratios and neglect the estimation of data quality of about 0.01% or better. Reproduced with permission from Chantler *et al.* (2015). Copyright 2015 International Union of Crystallography.

6.1.1. EXAFS data extraction for transmission and fluorescence measurements. XAS spectra of frozen solutions of Ni-^{n}Pr-Sal and Ni-^{i}Pr-Sal using an acetonitrile (40%)/butyronitrile (60%) mixed solvent contained in a multiposition solution cell allow the measurement of samples with differing concentrations together with the requisite background blank channels. Corrections for the transmittance spectra followed the approach shown in Fig. 2 and the resulting spectra for 15 and 1.5 m*M* solutions of pure (Ni-^{n}Pr-Sal) at $T = 80$ K together with the point-by-point estimate of errors of order 0.01% are given in Fig. 4.

Measurements of the fluorescence have been normalized and statistical analysis conducted in the manner outlined in Section 5.6 and this provides $[\mu/\rho]$ values and their associated uncertainties, which are consistent with the transmission measurements. In addition to the hybrid measurements, which give data with high point accuracy (HPA), a more conventional XAS scan was conducted to give a data set with high point density (HPD). In this case the measurements with HPA can be used to provide corrections for the HPD data and, for the fluorescence measurements, statistical analysis of the spectra obtained from the multi-element detector (Section 5.6) allows a statistically based assessment of the point-by-point uncertainty (Fig. 5).

6.1.2. XANES analysis. The logical starting point for the analysis is to focus on the pre-edge structure, where the intensity of the 1*s*–3*d* transition is expected to be significantly more intense for the noncentrosymmetric tetrahedral form. While this expectation is reflected in the XANES of tetrahedral and octahedral cobalt(II) complexes (Best, Kolev *et al.*, 2016) and of high-valent chromium complexes (Harris *et al.*, 2005; Parsons *et al.*, 2007), the spectra of Ni-^{n}Pr-Sal and Ni-^{i}Pr-Sal have pre-edge features of similar intensity (Fig. 6). Differences in the pre-edge and edge spectra are indicative of differences in the geometry of the two isomers in the solution

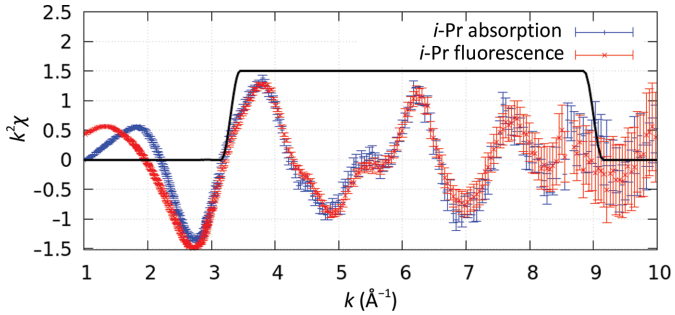

Figure 5
Transmission versus fluorescence spectra from Schalken & Chantler (2018). An excellent agreement is found between the two spectra within the Hanning window, indicative of the success of the self-absorption correction methodology. Some discrepancies remain between the two spectra, particularly in the application of background subtraction, edge removal and spline removal, an observation made possible by propagation of statistically robust experimental uncertainties.

Table 2
Summary of the main refinement parameters obtained using *IFEFFIT*-like (*eFEFFIT*) analysis of the transmission EXAFS data from Ni-^{i}Pr-Sal and Ni-^{n}Pr-Sal.

	Ni-^{i}Pr-Sal data; XRD or $\varphi = 90°$ models					Ni-^{n}Pr-Sal data; XRD or $\varphi = 0°$ models				
Model	E_0 (eV)	S_0^2	α	σ^2 (μm^2)	χ_r^2	E_0 (eV)	S_0^2	α	σ^2 (μm^2)	χ_r^2
XRD_{opt}†	−2.6 (1.0)	1.27 (0.31)	1.0010 (0.0003)	0.005 (0.003)	5.47	−2.9 (1.3)	1.31 (0.34)	1.048 (0.015)	0.010 (0.004)	6.17
Fig. 7, **A**‡	−8.6 (2.3)	0.98 (0.11)	0.990 (0.030)	0.005 (0.004)	6.82	−13.9 (6.5)	1.11 (0.31)	0.980 (0.020)	0.007 (0.005)	8.73
Fig. 7, **B**	−2.6 (1.3)	1.00 (0.11)	0.996 (0.006)	0.004 (0.003)	4.41	0.1 (1.4)	0.95 (0.13)	1.008 (0.007)	0.005 (0.003)	4.30
Fig. 7, **C**§	0.87 (1.16)	1.01 (0.03)	0.998 (0.003)	0.005 (0.002)	3.25	2.6 (1.5)	0.89 (0.04)	1.004 (0.006)	0.007 (0.003)	3.62
Fig. 7, **C***¶	0.62 (0.28)	1.02 (0.02)	1.001 (0.003)	0.003 (0.002)	2.94	2.3 (1.1)	0.91 (0.02)	1.007 (0.003)	0.006 (0.003)	3.27

† Structural parameters were obtained from the XRD crystal structures (Fox *et al.*, 1964; Britton & Pignolet, 1989) but with optimized Ni–O and Ni–N distances (using *eFEFFIT*). ‡ Optimized Ni–N and Ni–O distances; C–C and C–N distances and the N–Ni–O angle (93°) were based on the crystallographic database distribution function of similar groups. § Debye–Waller factors were independently refined for the Ni–O [0.0010 (5)] and Ni–N [0.0015 (1)] interactions. ¶ Extension of the model by adjustment of the N—Ni—O angle of the tetrahedral (89.2°) and square-planar (89.5°) species; the parameter α is the scale of bond lengths from the initial model structure.

state, but it is clear that a simple interpretation of the XANES is not sufficient to allow assignment of the geometry.

6.1.3. Modelling the EXAFS data. Owing to the limited extent of the EXAFS data, it is sensible first to consider the complexity of the model needed to give a good reproduction of the experimental observations. The simplest model is limited to the atoms that are directly bonded to the nickel absorber (region **A** in Fig. 7), where the inclusion of three-leg paths leads to differences in the computed EXAFS for the square-planar and tetrahedral forms. Inclusion of more atoms into the model by extending to regions **B** and **C** will increase the number of paths where, importantly, only the multiple-scattering paths involving both ligands in the calculated EXAFS will be sensitive to the rotation angle φ. The most simple structure refinement would use the crystallographically determined intra-ligand and metal–ligand bond lengths and optimize E_0, S_0^2, Debye–Waller factors and, possibly, a global scale factor for models with φ equal to 0° and 90°.

A summary of the refinement of the transmission EXAFS data from Ni-^{n}Pr-Sal and Ni-^{i}Pr-Sal is given in Table 2, where the reference point is a model based on the X-ray structures of the two compounds with optimization of the Ni–O and Ni–N distances. It is important to note that the refinement was conducted using a development of *iFEFFIT*, which takes account of the uncertainties associated with the individual data points (*eFEFFIT*), and the χ_r^2 values are statistically based and are not directly comparable with the conventional EXAFS analysis normalization (Islam *et al.*, 2015). There are several points that can be made from an analysis of differences or improvements of refinement parameters (Table 2). Firstly, the statistical significance of changes to the complexity of the model are much more clearly articulated through a properly determined value of χ_r^2. Secondly, the small differences in bond lengths associated with a change in state (from crystal XRD to solution XAFS) show up strongly in the XAFS, so care and insight needs to be exercised when transferring or evolving bond-length data from crystal to solution. Thirdly, fragmentary models can provide a useful way of identifying the parts of the structure that are most critical for analysis. Clearly, it is important that the model fragment has sufficient complexity to capture the main contributions to the XAFS. Here, the contributions of the first, second and third shells are

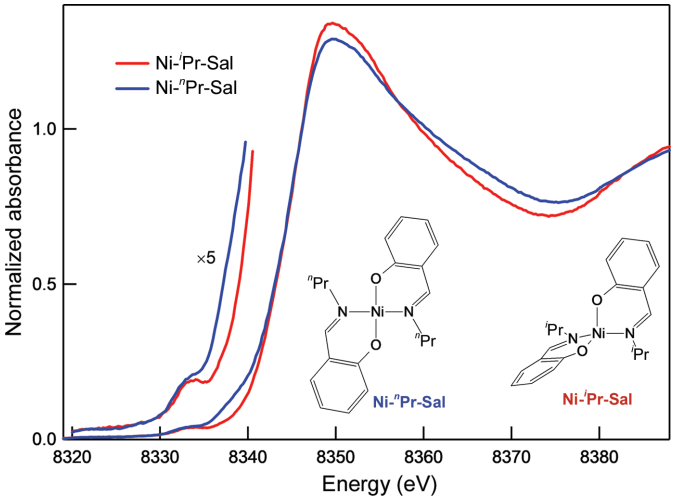

Figure 6
Ni-^{n}Pr-Sal and Ni-^{i}Pr-Sal in the pre-edge and edge regions. The relative intensities of the 1*s*–3*d* pre-edge transitions do not give a clear assignment of the geometry.

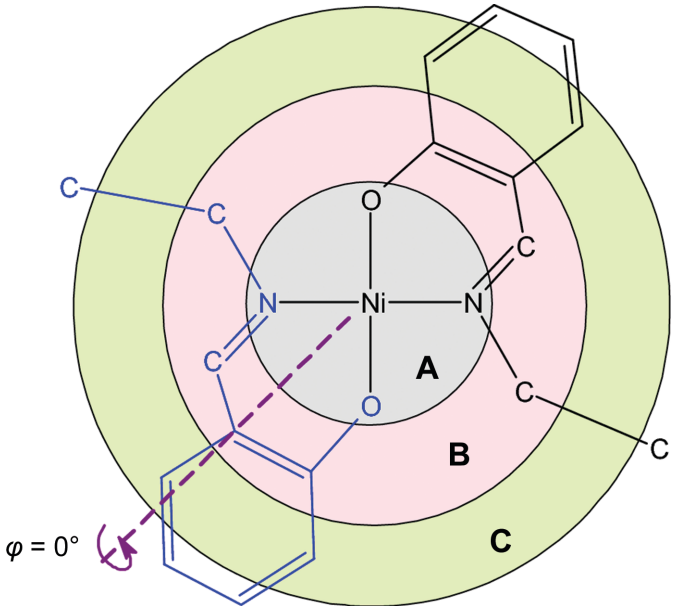

Figure 7
Models of increasing complexity can be constructed using the atoms bounded within regions **A**, **B** and **C**. The H atoms are assumed to make an insignificant contribution to the spectra and are omitted from the models. Distortion from the square-planar geometry (shown) to tetrahedral involves a rotation of the plane of one of the bidentate ligands (φ) by 90°. The two bidentate ligands are assumed to have identical geometries.

significant, and the symmetrized structure gives at least as good a fit of the solution-state EXAFS as the solid-state X-ray structure. It is well known that $\chi^2_r > 1$ is a consequence of (i) poor estimates or underestimates of point uncertainty, (ii) a loss of information in interpolation of data or transformation to the fitting axis of $\chi(k)$ or $\chi(r)$ and (iii) a poor or incomplete theoretical model encompassing the parameterization of the nuclear and thermal coordinates (see Abe, 2024; Booth, 2024*a*,*b*; Newville, 2024; Kubacka & Fernández-Garcia, 2024). It is also common that a 'significant' reduction in χ^2_r is indicative of a significantly better structure, model, theory *etc*. and this is in part formalized by the F-test, amongst others, which characterizes the χ^2 difference relative to the change of the number of degrees of freedom (see Booth, 2024*a*; Newville, 2024; Timoshenko & Kuzmin, 2024; Krappe *et al.*, 2024).

It is well understood that the complexity of model able to be supported by XAFS analysis is dependent on the quality and the extent of the experimental data, and for dilute samples fluorescence measurements can offer significant advantages. EXAFS analysis using fluorescence measurements collected from the same sample with HPA and HPD have been shown to support a more nuanced analysis, with a 2D parameter search giving optimized Ni—O and Ni—N bond distances and O—N—N angle. The optimized model provides a basis for evaluating the solution structures of the Ni-^{n}Pr-Sal and Ni-^{i}Pr-Sal complexes, where differences in the fits of the experimental data to the $\varphi = 0°$ and 90° models allow a statistically based assignment of the structure (Fig. 8; Schalken & Chantler, 2018). While it is apparent that there is a distortion of the EXAFS data for both compounds in the range 8.5–9 Å^{-1}, there is a clear distinction between the fits of the EXAFS of the two compounds to either the $\varphi = 0°$ or 90° models, allowing the assignment of Ni-^{n}Pr-Sal to a distorted square-planar geometry and Ni-^{i}Pr-Sal to a distorted tetrahedral geometry. Further, there are significant distortions of the solid-state structures for the complexes in solution. The most important outcome from this analysis is that the differences in geometry can be assessed from a solid statistical basis and that improvements in the beamline and the time available for the measurement of spectra will lead to quantifiable improvements in the quality of the data, which then translates into more precise and reliable structure determination.

6.2. Case 2: ferrocene, bis(cyclopentadienyl)iron(II) and decamethylferrocene

Ferrocene (Fc) is an example of a high-symmetry molecule which has long been a focus of fascination for reasons related to its electronic and molecular structure (Dunitz, 1993; Coriani *et al.*, 2006). Fc was the first example of side-on bonding of the delocalized orbitals of an aromatic molecule to a transition metal, a motif that is common among organometallic compounds and catalytic systems. The delocalized bonding within the molecule underlies its well defined redox chemistry,

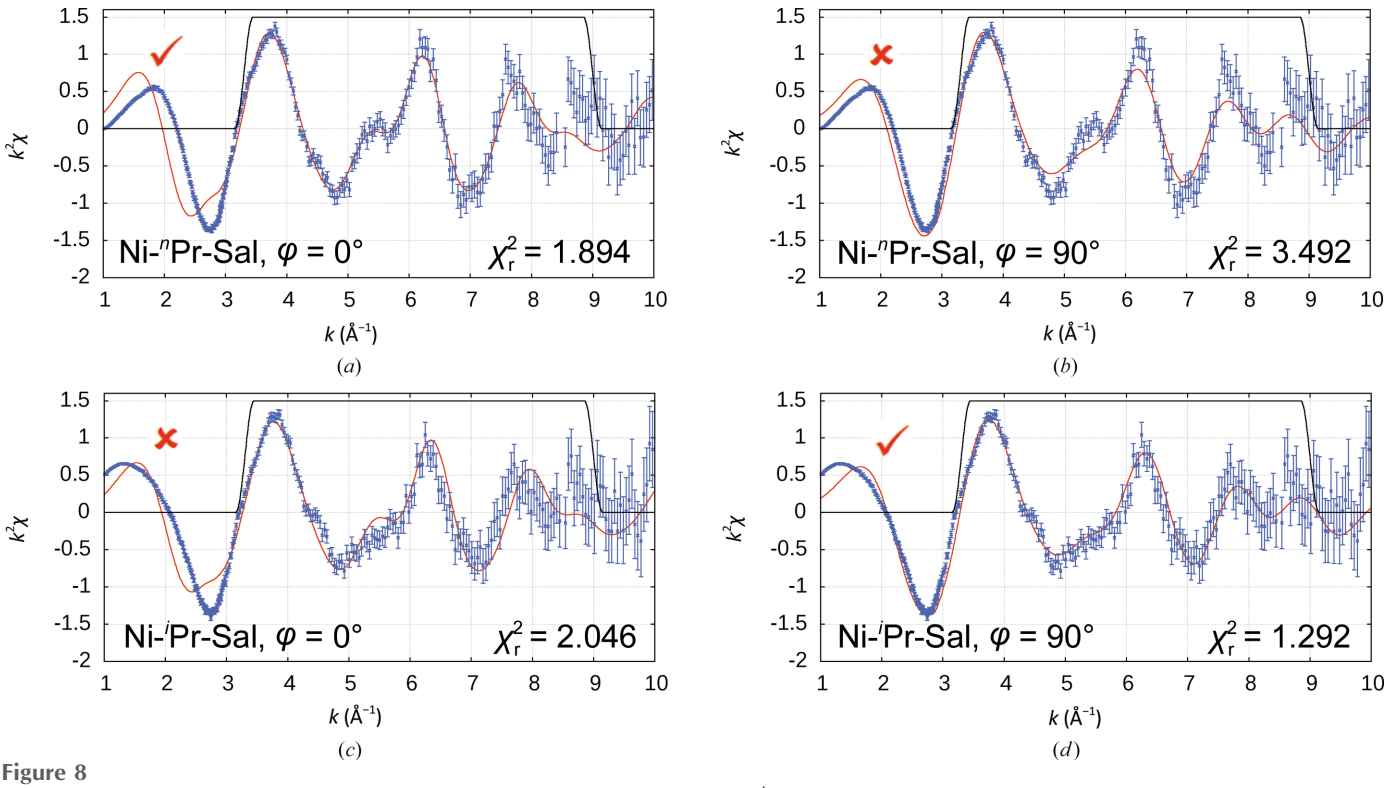

Figure 8
High-point-density fluorescence EXAFS of frozen solutions of Ni-^{n}Pr-Sal and Ni-^{i}Pr-Sal fitted to the optimized 'square-planar' ($\varphi = 0°$) or optimized 'tetrahedral' ($\varphi = 90°$) geometry. The data, model and χ^2_r are indicated for each of the *eFEFFIT* fits. It is clear that the actual uncertainties are not uniform in χ space or in $k^2\chi$ space but are in general much smaller at low k, so that fits with defined uncertainties put a premium on accurate theory and experiment for lower k regions. Reproduced with permission from Schalken & Chantler *et al.* (2018). Copyright 2018 International Union of Crystallography.

a property exploited in sensors such as glucose monitors (Sakakida *et al.*, 1993). The structure of Fc can be described in terms of the high-symmetry rotameric forms differing according to the relative orientation of the two cyclopentadienyl (Cp) rings. When viewed along the fivefold axis, the Cp rings may adopt a staggered conformation to give a molecule with D_{5d} symmetry or an eclipsed conformation with D_{5h} molecular symmetry. Phase transitions, static and dynamic disorder complicate the interpretation of the crystallography (Fischer & Pfab, 1952; Wilkinson *et al.*, 1952), but all phases can be interpreted in terms of a disordered ensemble of molecules individually of D_{5h} symmetry (Seiler & Dunitz, 1979). The low barrier to interconversion between the D_{5h} and D_{5d} forms, first quantified as 1–2 kJ mol^{-1} by gas-phase electron diffraction measurements (Haaland & Nilsson, 1968), is a feature of the molecules in all phases (Freyberg *et al.*, 1979; Best, Wang *et al.*, 2016; Struchkov *et al.*, 1978). A staggered (D_{5d}) conformation of the C_5 rings can be achieved by replacement of the Cp rings by pentamethylcyclopentadienyl (Cp*) groups (Mochida & Yoza, 2010; Sanjuan-Szklarz *et al.*, 2016). Decamethylferrocene (DMFc) is available to provide a companion system with its staggered isomeric structure dictated by steric forces. Thus, Fc and DMFc present the opportunity to study both isomerism and molecular dynamics.

Fc represents an extremely challenging problem for EXAFS. In common with the Ni-Pr-Sal complexes, the differences in EXAFS between the isomeric forms are only in terms of multiple-scattering interactions. For Fc the differences in scattering paths are subtle, as conversion between the D_{5h} and D_{5d} forms is associated with a relative rotation of the Cp rings by 36°, and this is reflected by small differences in the calculated EXAFS of the isomeric forms (Bourke, Islam *et al.*, 2016). In this example discrimination between the alternate isomeric forms is a very serious test of both theory and data quality. Indeed, the two-leg paths are identical and the signature differences arise from three-leg and higher *n*-leg paths and remain a small percentage of the total interference signal.

Interestingly, there have been two good prior studies of Fc using XAFS. The first (Cramer *et al.*, 1976) compared the structural effects of background removal rather than a detailed determination of the structure or conformer. The second (Ruiz-Lopez *et al.*, 1988) used muffin-tin theory similar to current popular approaches, with apparently much higher data quality. However, they found no theoretical difference between the conformer XAFS paths or theoretical predictions and therefore concluded that (based on the available data) it was impossible to distinguish the conformers even if one were significantly more stable.

XAS measurements of frozen solutions of Fc and DMFc [15 and 3 m*M* in acetonitrile (40%):butyronitrile (60%)] were conducted using the protocols described for Ni-Pr-Sal (Section 6.1; Bourke, Islam *et al.*, 2016; Islam *et al.*, 2016). Model building for Fc can take the form of the reported crystal structure with a relative rotation of one of the Cp rings to generate approximate D_{5h} and D_{5d} forms, or the nuclear coordinates can be used to generate the coordinates of the single, independent C and H atoms needed to construct a high-symmetry molecule in either isomeric form. Whilst models based on the crystal structure coordinates for the D_{5h} geometry gave refinements which were satisfactory (χ^2_r values of 3.97–3.99), significantly better fits were obtained using high-symmetry regularized structures (χ^2_r values of 3.44 and 3.28), which were further improved by *eFEFFIT* refinement of the ratio of the Fe—C and C—C bond lengths (χ^2_r = 3.17), and the addition of a separate Debye–Waller factor for the H atom (χ^2_r = 3.06) results in further small improvements to the fit (Islam *et al.*, 2016). A similar approach applied to DMFc returned χ^2_r values of 4.15 using models based on the X-ray structures which were regularized (C_5 symmetry of the Cp* rings) and refined (Islam *et al.*, 2016). The poorer DMFc fit may relate to a loss of C_5 symmetry from distortions due to steric repulsions between methyl groups.

The question concerning the conformation of Fc and DMFc is subtle and in view of the similarity of the calculated EXAFS for the D_{5h} and D_{5d} forms (Fig. 9) it is unsurprising that the differences in the refinement statistics are small. Whilst the lower χ^2_r values are obtained for the D_{5h} form for Fc and the D_{5d} form for DMFc are consistent with expectations, these

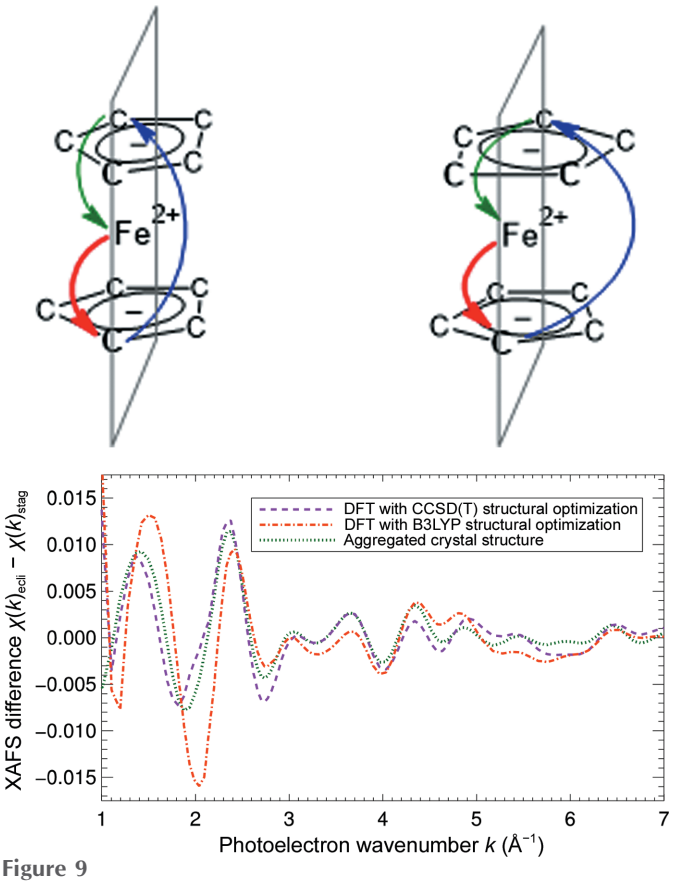

Figure 9
Top: the near-linear three-leg multiple-scattering paths for the D_{5h} (left) and D_{5d} (right) forms of Fc (for clarity, H atoms are not shown). Similar three-leg paths can be formed which involve each of the five C atoms of the top Cp ring. Bottom: calculated EXAFS for the D_{5h} and D_{5d} forms of Fc. Structures were based either on X-ray structure determinations or *ab initio* density-functional theory calculations with different functional optimizations. Reproduced with permission from Bourke *et al.* (2016). Copyright 2016 American Chemical Society.

Table 3
Goodness of fit for eclipsed and staggered conformers based on prototype geometries over different k-ranges.

ACS refers to the aggregated crystal structure reported in Islam *et al.* (2016) and derived as a refinement of the structure given by Seiler & Dunitz (1979). Note that within each k-range the core parameters were optimized. The best-fit geometry is identified in cases where $|\chi_r^2(D_{5h}) - \chi_r^2(D_{5d})| > 1$ and is indicated by *. These are suggestive or conclusive determinations, whilst other subsets are inconclusive.

	χ_r^2		
Fc			
k-range (Å^{-1})	1.0–3.0	1.0–7.0	3.0–7.0
CCSD(T), D_{5h}	14.4*	14.3	7.43
CCSD(T), D_{5d}	19.6	14.0	7.01
B3LYP, D_{5h}	20.1*	24.4*	5.12
B3LYP, D_{5d}	35.2	35.2	5.14
ACS, D_{5h}	12.8*	14.0*	8.02
ACS, D_{5d}	17.0	15.6	8.01
DMFc			
k-range (Å^{-1})	1.5–3.5	1.5–7.0	3.5–7.0
Islam *et al.* (2016), D_{5h}	9.02	11.4	6.37
Islam *et al.* (2016), D_{5d}	8.16	10.4*	5.76
Makal *et al.* (2010), D_{5h}	7.69	6.71	3.49
Makal *et al.* (2010), D_{5d}	6.91	5.32*	2.97

differences are only suggestive and it is difficult to discern model-dependent systematic differences from inspection of the calculated and observed EXAFS (Fig. 10). A frustrating element of conventional *FEFF* analysis is that the data with the greatest information content are at low k, where this region has both the largest contribution from multiple-scattering contributions and the smallest relative error of the measurement. Data within the k-range below 3 or 3.5 Å^{-1} are, however, those most poorly defined by standard theory.

A limitation of EXAFS analysis based on calculations conducted within a 'muffin-tin' approximation of the inter-atomic potential is a failure to accurately model the EXAFS in the low-k region (k < 3–3.5 Å^{-1}), this being critical to the stereochemical analysis of Fc. Full potential modelling, conducted within a quantum-mechanical framework, is needed to address the problem. Finite-difference methods (FDMs) have been developed to allow the modelling of XANES (*FDMNES*; FDM near-edge structure; Bunău & Joly, 2009; Bourke & Chantler, 2010; Guda *et al.*, 2015). More recently, this has been extended into the *FDMX* package to fit the EXAFS range (Bourke, Chantler *et al.*, 2016). Although very subtle, small differences in the shape of the first oscillations of the EXAFS are evident for *FDMX* calculations of the D_{5h} and D_{5d} conformers of Fc (Fig. 11; Bourke, Islam *et al.*, 2016). The excellent agreement between the *FDMX*-calculated EXAFS and experiment supports extension of the analysis to k = 1 Å^{-1}; however, statistical evaluation of the difference between the structural models relies heavily on a reliable assessment of the uncertainty of the individual measurements as is provided by the hybrid approach.

The *FDMX* approach is much more computationally demanding than *FEFF*-based approaches and analogous least-squares parameter optimization is challenging. The approach taken to assess the performance of D_{5h}-type and D_{5d}-type models has been to calculate the goodness of fit of computationally or X-ray structure-derived models of Fc and DMFc and assess their relative merits over different regions of k-space (Table 3). The structure of Fc derived from DFT with the B3LYP functional returns the lowest value of χ_r^2 if the

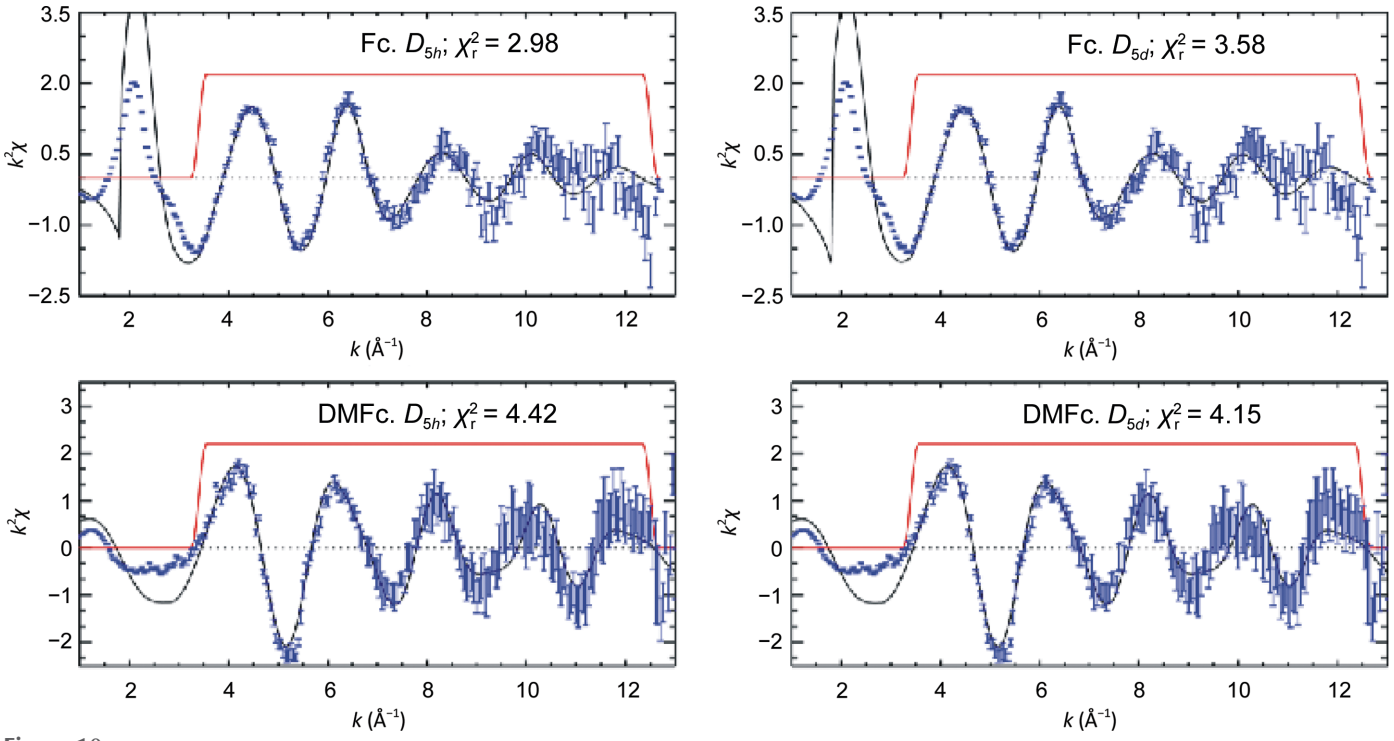

Figure 10
k^2-weighted EXAFS spectra of Fc (upper row) and DMFc (lower row) using eclipsed (left) and staggered (right) models of the geometry. The experimental conditions and values of χ_r^2 are explained in Islam *et al.* (2016). The fit of the DMFc data above k = 9 Å may be limited by the constraint that the Cp* ring have C_5 symmetry. Modified with permission from Islam *et al.* (2016). Copyright 2016 American Chemical Society.

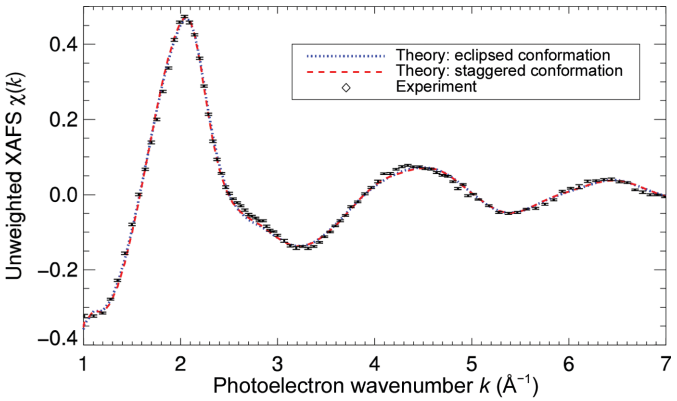

Figure 11
$\chi(k)$ XAFS spectra of ferrocene using eclipsed and staggered conformations based on the aggregated crystal structure. Differences lie mainly at lower k from multiple-leg paths. Reproduced with permission from Bourke *et al.* (2016). Copyright 2016 American Chemical Society.

k-range is between 3 and 7 Å^{-1} and is highly sensitive to the conformation in the range 1–3 Å^{-1}. This difference relates to the relative importance of single- and multiple-scattering contributions to the EXAFS in the different k-ranges. In terms of the structural question relating to Fc, it is most significant that for the low-k data the χ^2_r values are significantly lower for the D_{5h} conformer of Fc for all of the models considered. This conclusion is consistent with a broad range of independent experimental and theoretical conclusions and, most importantly, the comparative performance of the models based on the D_{5h} and D_{5d} geometries appears not to be dependent on small differences in the geometric details of the model; for example, the internuclear contacts differ for the CCSD(T), B3LYP and ACS models. Further, refinement of the EXAFS of DMFc leads to a small, but now significant, preference for the expected staggered D_{5d} conformation. Central to the development of the approach is a strong statistical basis for the evaluation of the performance of the different models, where this depends on the measurement of data with well defined precision and relative accuracy.

7. Conclusions and summary

A key objective of any experimental study is to maximize the quality of the measured data, yet there is lively discussion over the importance placed on the correction of XAS data for systematic errors and the quantification of errors. In some measure both issues may be traced back to the necessity to subtract the background associated with photoionization of an isolated atom to yield the EXAFS. If the effect of systematic errors is a slowly changing function with energy, then it may be argued that background subtraction will additionally remove the effects of systematic errors. Such an approach runs the risk of introducing distortions into the spectra and removing the possibility of measurement-based estimates of the point-by-point uncertainties of the data. Hybrid approaches occupy the space between measurements with no point-by-point estimate of the uncertainty through to high-accuracy measurements with defined errors for the individual measurements. For dilute samples in disordered environments the collection of high-quality EXAFS with statistically defined precision remains a challenging undertaking that will surely become more important as methods for *ab initio* calculation of spectra in the XANES/XAFS interface develop. The measurement of spectra using either transmission or fluorescence detection can be a vexed question. While the correction of systematics is more straightforward for transmission measurements, the multi-element detectors commonly used for the collection of fluorescent X-rays in XAS measurements provide multiple independent measurements of the spectrum which can also be used to quantify the statistical reliability of the measurement. In order to take advantage of this opportunity it is necessary to make corrections both for the gain of the individual elements and to account for processes such as self-absorption.

For fields such as catalysis the elucidation of subtle details of the molecular structure around the metal can be critical to understanding the relationship between molecular structure, electronic structure and reactivity, and the case for the application of methods which lead to structural answers with quantifiable reliability is clear. However, irrespective of the application, better science is obtained on the back of better data.

References

Abd el All, N., Thiodjio Sendja, B., Grisenti, R., Rocca, F., Diop, D., Mathon, O., Pascarelli, S. & Fornasini, P. (2013). *J. Synchrotron Rad.* **20**, 603–613.
Abe, H. (2024). *Int. Tables Crystallogr. I*, ch. 4.2, 594–599.
Babanov, Y. A., Ryazhkin, A. V. & Miyanaga, T. (2001). *Nucl. Instrum. Methods Phys. Res. A*, **470**, 278–282.
Barnea, Z., Chantler, C. T., Glover, J. L., Grigg, M. W., Islam, M. T., de Jonge, M. D., Rae, N. A. & Tran, C. Q. (2011). *J. Appl. Cryst.* **44**, 281–286.
Barnea, Z. & Mohyla, J. (1974). *J. Appl. Cryst.* **7**, 298–299.
Benelli, C., Bertini, I. & Gatteschi, D. (1972). *J. Chem. Soc. Dalton Trans.*, pp. 661–663.
Best, S. P., Kolev, S. D., Gabriel, J. R. P. & Cattrall, R. W. (2016). *J. Membr. Sci.* **497**, 377–386.
Best, S. P., Wang, F., Islam, M. T., Islam, S., Appadoo, D., Trevorah, R. M. & Chantler, C. T. (2016). *Chem. Eur. J.* **22**, 18019–18026.
Booth, C. H. (2024*a*). *Int. Tables Crystallogr. I*, ch. 5.8, 672–675.
Booth, C. H. (2024*b*). *Int. Tables Crystallogr. I*, ch. 5.9, 676–677.
Booth, C. H. & Bridges, F. (2005). *Phys. Scr.* **2005**, 202.
Bourke, J. D. & Chantler, C. T. (2010). *Nucl. Instrum. Methods Phys. Res. A*, **619**, 33–36.
Bourke, J. D., Chantler, C. T. & Joly, Y. (2016). *J. Synchrotron Rad.* **23**, 551–559.
Bourke, J. D., Islam, M. T., Best, S. P., Tran, C. Q., Wang, F. & Chantler, C. T. (2016). *J. Phys. Chem. Lett.* **7**, 2792–2796.
Bridges, F. (2024*a*). *Int. Tables Crystallogr. I*, ch. 3.13, 370–374.
Bridges, F. (2024*b*). *Int. Tables Crystallogr. I*, ch. 3.41, 546–548.
Britton, D. & Pignolet, L. H. (1989). *Acta Cryst.* C**45**, 819–821.
Bunău, O. & Joly, Y. (2009). *J. Phys. Condens. Matter*, **21**, 345501.
Bunker, G. (2010). *Introduction to XAFS: A Practical Guide to X-ray Absorption Fine Structure Spectroscopy.* Cambridge University Press.
Bunker, G. (2024*a*). *Int. Tables Crystallogr. I*, ch. 3.16, 400–403.
Bunker, G. (2024*b*). *Int. Tables Crystallogr. I*, ch. 3.45, 567–571.
Bunker, G. (2024*c*). *Int. Tables Crystallogr. I*, ch. 5.3, 639–644.
Bunker, G. (2024*d*). *Int. Tables Crystallogr. I*, ch. 5.2, 636–638.

Calvin, S. (2013). *XAFS for Everyone*, 1st ed. Boca Raton: CRC Press.
Chantler, C. T. (1995). *J. Phys. Chem. Ref. Data*, **24**, 71–643.
Chantler, C. T. (2000). *J. Phys. Chem. Ref. Data*, **29**, 597–1056.
Chantler, C. T. (2001). *Radiat. Phys. Chem.* **61**, 343–345.
Chantler, C. T. (2009). *Eur. Phys. J. Spec. Top.* **169**, 147–153.
Chantler, C. T. (2024). *Int. Tables Crystallogr. I*, ch. 3.38, 537–538.
Chantler, C. T., Barnea, Z., Tran, C. Q., Rae, N. A. & de Jonge, M. D. (2012). *J. Synchrotron Rad.* **19**, 851–862.
Chantler, C. T., Barnea, Z., Tran, C. Q., Tiller, J. B. & Paterson, D. (1999). *Opt. Quant. Electron.* **31**, 495–505.
Chantler, C. T., Islam, M. T., Best, S. P., Tantau, L. J., Tran, C. Q., Cheah, M. H. & Payne, A. T. (2015). *J. Synchrotron Rad.* **22**, 1008–1021.
Chantler, C. T., Islam, M. T., Rae, N. A., Tran, C. Q., Glover, J. L. & Barnea, Z. (2012). *Acta Cryst.* A**68**, 188–195.
Chantler, C. T., Rae, N. A., Islam, M. T., Best, S. P., Yeo, J., Smale, L. F., Hester, J., Mohammadi, N. & Wang, F. (2012). *J. Synchrotron Rad.* **19**, 145–158.
Chantler, C. T., Tran, C. Q., Paterson, D., Barnea, Z. & Cookson, D. J. (2000). *X-ray Spectrom.* **29**, 449–458.
Chantler, C. T., Tran, C. Q., Paterson, D., Cookson, D. J. & Barnea, Z. (2000). *X-ray Spectrom.* **29**, 459–466.
Ciatto, G., Fonda, E. & Maurizio, C. (2024). *Int. Tables Crystallogr. I*, ch. 4.4, 606–612.
Coriani, S., Haaland, A., Helgaker, T. & Jørgensen, P. (2006). *ChemPhysChem*, **7**, 245–249.
Cramer, S. P., Eccles, T. K., Kutzler, F., Hodgson, K. O. & Doniach, S. (1976). *J. Am. Chem. Soc.* **98**, 8059–8069.
Creagh, D. C. & Hubbell, J. H. (1987). *Acta Cryst.* A**43**, 102–112.
Creagh, D. C. & Hubbell, J. H. (1990). *Acta Cryst.* A**46**, 402–408.
Curis, E., Osán, J., Falkenberg, G., Bénazeth, S. & Török, S. (2005). *At. Spectrosc.* **60**, 841–849.
d'Acapito, F. (2024). *Int. Tables Crystallogr. I*, ch. 4.5, 613–616.
de Jonge, M. D., Barnea, Z., Tran, C. Q. & Chantler, C. T. (2004*a*). *Meas. Sci. Technol.* **15**, 1811–1822.
de Jonge, M. D., Barnea, Z., Tran, C. Q. & Chantler, C. T. (2004*b*). *Phys. Rev. A*, **69**, 022717.
de Jonge, M. D., Tran, C. Q., Chantler, C. T., Barnea, Z., Dhal, B. B., Cookson, D. J., Lee, W.-K. & Mashayekhi, A. (2005). *Phys. Rev. A*, **71**, 032702.
De Panfilis, S. & Bardelli, F. (2024). *Int. Tables Crystallogr. I*, ch. 4.3, 600–605.
Diaz-Moreno, S. (2012). *J. Synchrotron Rad.* **19**, 863–868.
Diaz-Moreno, S. & Boada, R. (2022). *Int. Tables Crystallogr. I*, ch. 3.7, 321–327.
Diaz-Moreno, S. & Strange, R. W. (2018). *J. Synchrotron Rad.* **25**, 918–919.
Dunitz, J. D. (1993). *Organic Chemistry: Its Language and Its State of the Art*, edited by M. V. Kisakürek, pp. 9–23. Basel: Verlag Helvetica Chimica Acta.
Eisebitt, S., Böske, T., Rubensson, J. E. & Eberhardt, W. (1993). *Phys. Rev. B*, **47**, 14103–14109.
Filipponi, A., Di Cicco, A. & Natoli, C. R. (2024). *Int. Tables Crystallogr. I*, ch. 6.12, 787–790.
Filipponi, A., Natoli, C. R. & Di Cicco, A. (2024). *Int. Tables Crystallogr. I*, ch. 6.11, 782–786.
Fischer, E. O. & Pfab, W. (1952). *Z. Naturforsch. B*, **7**, 377–379.
Fornasini, P. (2024). *Int. Tables Crystallogr. I*, ch. 5.11, 683–686.
Fox, M. R., Lingafelter, E. C., Orioli, P. L. & Sacconi, L. (1963). *Nature*, **197**, 1104.
Fox, M. R., Orioli, P. L., Lingafelter, E. C. & Sacconi, L. (1964). *Acta Cryst.* **17**, 1159–1166.
Freyberg, D. P., Robbins, J. L., Raymond, K. N. & Smart, J. C. (1979). *J. Am. Chem. Soc.* **101**, 892–897.
Fujikawa, T. (2024). *Int. Tables Crystallogr. I*, ch. 2.5, 60–70.
Gianolio, D., Borfecchia, E., Garino, C., Ruiu, T., Lamberti, C. & Salassa, L. (2013). *J. Phys. Conf. Ser.* **430**, 012125.
Glatzel, P., Juhin, A. & Moretti, M. (2024). *Int. Tables Crystallogr. I*, ch. 2.19, 177–189.
Glover, J. L. & Chantler, C. T. (2009). *X-ray Spectrom.* **38**, 510–512.
Glover, J. L., Chantler, C. T., Barnea, Z., Rae, N. A. & Tran, C. Q. (2010). *J. Phys. B At. Mol. Opt. Phys.* **43**, 085001.
Glover, J. L., Chantler, C. T. & de Jonge, M. D. (2009). *Phys. Lett. A*, **373**, 1177–1180.
Goulon, J., Goulon-Ginet, C., Cortes, R. & Dubois, J. M. (1982). *J. Phys. Fr.* **43**, 539–548.
Guda, S. A., Guda, A. A., Soldatov, M. A., Lomachenko, K. A., Bugaev, A. L., Lamberti, C., Gawelda, W., Bressler, C., Smolentsev, G., Soldatov, A. V. & Joly, Y. (2015). *J. Chem. Theory Comput.* **11**, 4512–4521.
Haaland, A. & Nilsson, J.-E. (1968). *Chem. Commun.*, pp. 88–89.
Harris, H. H., Levina, A., Dillon, C. T., Mulyani, I., Lai, B., Cai, Z. & Lay, P. A. (2005). *J. Biol. Inorg. Chem.* **10**, 105–118.
Hayakawa, S., Gohshi, Y., Iida, A., Aoki, S. & Sato, K. (1991). *Rev. Sci. Instrum.* **62**, 2545–2549.
Heald, S. (2024). *Int. Tables Crystallogr. I*, ch. 3.19, 416–421.
Hill, H. A. O., Horsler, A. D. J. & Sadler, P. J. (1973). *J. Chem. Soc. Dalton Trans.*, pp. 1805–1809.
Holm, R. H. & Swaminathan, K. (1963). *Inorg. Chem.* **2**, 181–186.
Iida, A. & Noma, T. (1993). *Jpn. J. Appl. Phys.* **32**, 2899–2902.
Islam, M. T., Best, S. P., Bourke, J. D., Tantau, L. J., Tran, C. Q., Wang, F. & Chantler, C. T. (2016). *J. Phys. Chem. C*, **120**, 9399–9418.
Islam, M. T., Chantler, C. T., Cheah, M. H., Tantau, L. J., Tran, C. Q. & Best, S. P. (2015). *J. Synchrotron Rad.* **22**, 1475–1491.
Jaklevic, J., Kirby, J. A., Klein, M. P., Robertson, A. S., Brown, G. S. & Eisenberger, P. (1977). *Solid State Commun.* **23**, 679–682.
Jaklevic, J., Kirby, J. A., Klein, M. P., Robertson, A. S., Brown, G. S. & Eisenberger, P. (1993). *Solid State Commun.* **88**, 1105–1108.
Kavčič, M. & Žitnik, M. (2024). *Int. Tables Crystallogr. I*, ch. 5.5, 653–658.
Knorr, R., Hauer, H., Weiss, A., Polzer, H., Ruf, F., Löw, P., Dvortsák, P. & Böhrer, P. (2007). *Inorg. Chem.* **46**, 8379–8390.
Koningsberger, D. C. & Prins, R. (1988). *X-ray Absorption: Principles, Applications, Techniques of EXAFS, SEXAFS and XANES.* Chichester: John Wiley & Sons.
Krappe, H. J., Holub-Krappe, E., Konishi, T. & Rossner, H. H. (2024). *Int. Tables Crystallogr. I*, ch. 5.15, 702–704.
Krappe, H. J. & Rossner, H. (1999). *J. Synchrotron Rad.* **6**, 302–303.
Krappe, H. J. & Rossner, H. H. (2000). *Phys. Rev. B*, **61**, 6596–6610.
Krappe, H. J. & Rossner, H. H. (2002). *Phys. Rev. B*, **66**, 184303.
Krappe, H. J. & Rossner, H. H. (2004). *Phys. Rev. B*, **70**, 104102.
Kubacka, A. & Fernández-Garcia, M. (2024). *Int. Tables Crystallogr. I*, ch. 5.18, 716–719.
Lawniczak-Jablonska, K. (2024). *Int. Tables Crystallogr. I*, ch. 3.20, 422–426.
Lee, P. A., Citrin, P. H., Eisenberger, P. & Kincaid, B. M. (1981). *Rev. Mod. Phys.* **53**, 769–806.
Li, G. G., Bridges, F. & Wang, X. (1994). *Nucl. Instrum. Methods Phys. Res. A*, **340**, 420–426.
Liu, J. & Frenkel, A. I. (2024). *Int. Tables Crystallogr. I*, ch. 5.4, 645–652.
Lu, K., Wan, J., Zhao, Y., Chang, L. & Fang, Z. (1989). *Physica B*, **158**, 273–275.
Makal, A. M., Plażuk, D., Zakrzewski, J., Misterkiewicz, B. & Woźniak, K. (2010). *Inorg. Chem.* **49**, 4046–4059.
Meitzner, G. D. & Fischer, D. A. (2002). *Microchem. J.* **71**, 281–286.
Mochida, T. & Yoza, K. (2010). *J. Organomet. Chem.* **695**, 1749–1752.
Newville, M. (2001*a*). *J. Synchrotron Rad.* **8**, 96–100.
Newville, M. (2001*b*). *J. Synchrotron Rad.* **8**, 322–324.
Newville, M. (2024). *Int. Tables Crystallogr. I*, ch. 5.13, 690–694.
Nordfors, B. (1960). *Ark. Fys.* **18**, 37–47.
Ovsyannikov, P. M. & Shuvaev, A. T. (1995). *Physica B*, **208–209**, 148–150.

Oyanagi, H. (1988). *NSLS Workshop*, 7 March 1988.
Parratt, L. G., Hempstead, C. F. & Jossem, E. L. (1957). *Phys. Rev.* **105**, 1228–1232.
Parsons, J. G., Dokken, K., Peralta-Videa, J. R., Romero-Gonzalez, J. & Gardea-Torresdey, J. L. (2007). *Appl. Spectrosc.* **61**, 338–345.
Pease, D. M. (1976). *Appl. Spectrosc.* **30**, 405–410.
Pease, D. M., Brewe, D. L., Tan, Z., Budnick, J. I. & Law, C. C. (1989). *Phys. Lett. A*, **138**, 230–234.
Pettifer, R. F., Mathon, O., Pascarelli, S., Cooke, M. D. & Gibbs, M. R. J. (2005). *Nature*, **435**, 78–81.
Pfalzer, P., Urbach, J. P., Klemm, M., Horn, S., denBoer, M. L., Frenkel, A. I. & Kirkland, J. P. (1999). *Phys. Rev. B*, **60**, 9335–9339.
Rae, N. A., Glover, J. L. & Chantler, C. T. (2010). *Nucl. Instrum. Methods Phys. Res. A*, **619**, 47–50.
Ravel, B. & Newville, M. (2005). *J. Synchrotron Rad.* **12**, 537–541.
Ravel, B. & Newville, M. (2024). *Int. Tables Crystallogr. I*, ch. 6.1, 723–727.
Rehr, J. J., Kozdon, J., Kas, J., Krappe, H. J. & Rossner, H. H. (2005). *J. Synchrotron Rad.* **12**, 70–74.
Ruiz-Lopez, M. F., Loos, M., Goulon, J., Benfatto, M. & Natoli, C. R. (1988). *Chem. Phys.* **121**, 419–437.
Sacconi, L. (1966). *Coord. Chem. Rev.* **1**, 126–132.
Sacconi, L., Ciampolini, M. & Nardi, N. (1964). *J. Am. Chem. Soc.* **86**, 819–823.
Sacconi, L., Paoletti, P. & Ciampolini, M. (1963). *J. Am. Chem. Soc.* **85**, 411–416.
Sakakida, M., Nishida, K., Shichiri, M., Ishihara, K. & Nakabayashi, N. (1993). *Sens. Actuators B Chem.* **13**, 319–322.
Sanjuan-Szklarz, W. F., Hoser, A. A., Gutmann, M., Madsen, A. Ø. & Woźniak, K. (2016). *IUCrJ*, **3**, 61–70.
Schalken, M. J. & Chantler, C. T. (2018). *J. Synchrotron Rad.* **25**, 920–934.
Seiler, P. & Dunitz, J. D. (1979). *Acta Cryst.* B**35**, 1068–1074.
Stern, E. A. & Kim, K. (1981). *Phys. Rev. B*, **23**, 3781–3787.
Struchkov, Y. T., Andrianov, V. G., Sal'nikova, T. N., Lyatifov, I. R. & Materikova, R. B. (1978). *J. Organomet. Chem.* **145**, 213–223.
Sutter, J. P. (2024). *Int. Tables Crystallogr. I*, ch. 3.4, 290–301.
Sutter, J. P., Boada, R., Bowron, D. T., Stepanov, S. A. & Díaz-Moreno, S. (2016). *J. Appl. Cryst.* **49**, 1209–1222.
Suzuki, M. (2024). *Int. Tables Crystallogr. I*, ch. 3.10, 352–356.
Tan, Z., Budnick, J. I. & Heald, S. M. (1989). *Rev. Sci. Instrum.* **60**, 1021–1025.
Tantau, L. J., Chantler, C. T., Bourke, J. D., Islam, M. T., Payne, A. T., Rae, N. A. & Tran, C. Q. (2015). *J. Phys. Condens. Matter*, **27**, 266301.
Tantau, L. J., Islam, M. T., Payne, A. T., Tran, C. Q., Cheah, M. H., Best, S. P. & Chantler, C. T. (2014). *Radiat. Phys. Chem.* **95**, 73–77.
Timoshenko, J. & Kuzmin, A. (2024). *Int. Tables Crystallogr. I*, ch. 5.14, 695–701.
Tran, C. Q., Barnea, Z., de Jonge, M. D., Dhal, B. B., Paterson, D., Cookson, D. J. & Chantler, C. T. (2003). *X-ray Spectrom.* **32**, 69–74.
Tran, C. Q., Chantler, C. T., Barnea, Z. & de Jonge, M. D. (2004). *Rev. Sci. Instrum.* **75**, 2943–2949.
Tran, C. Q., Chantler, C. T., Barnea, Z., Paterson, D. & Cookson, D. J. (2003). *Phys. Rev. A*, **67**, 042716.
Tran, C. Q., Chantler, C. T. & de Jonge, M. D. (2024). *Int. Tables Crystallogr. I*, ch. 3.42, 549–557.
Tran, C. Q., de Jonge, M. D., Barnea, Z. & Chantler, C. T. (2004). *J. Phys. B At. Mol. Opt. Phys.* **37**, 3163–3176.
Trevorah, R. M., Chantler, C. T. & Schalken, M. J. (2019). *IUCrJ*, **6**, 586–602.
Tröger, L., Arvanitis, D., Baberschke, K., Michaelis, H., Grimm, U. & Zschech, E. (1992). *Phys. Rev. B*, **46**, 3283–3289.
Vaarkamp, M. (1998). *Catal. Today*, **39**, 271–279.
Webb, S. M. (2024). *Int. Tables Crystallogr. I*, ch. 5.17, 709–715.
Webb, S. M. & Gaillard, J. F. (2015). *Aquat. Geochem.* **21**, 295–312.
Westre, T. E., Di Cicco, A., Filipponi, A., Natoli, C. R., Hedman, B., Solomon, E. I. & Hodgson, K. O. (1995). *J. Am. Chem. Soc.* **117**, 1566–1583.
Wilkinson, G., Rosenblum, M., Whiting, M. C. & Woodward, R. B. (1952). *J. Am. Chem. Soc.* **74**, 2125–2126.
Zhang, H. H., Filipponi, A., Di Cicco, A., Lee, S. C., Scott, M. J., Holm, R. H., Hedman, B. & Hodgson, K. O. (1996). *Inorg. Chem.* **35**, 4819–4828.